



Computationally guided synthesis of (2D/3D/2D) rGO/Fe₂O₃/g-C₃N₄ nanostructure with improved charge separation and transportation efficiency for degradation of pharmaceutical molecules



Shajahan Shanavas^{a,*}, Selvaraj Mohana Roopan^{b,1}, Arumugam Priyadharsan^{a,1}, Duraipandi Devipriya^b, Selvam Jayapandi^c, Roberto Acevedo^d, Ponnusamy Munusamy Anbarasan^{a,*}

^a Nano and Hybrid Materials Laboratory, Department of Physics, Periyar University, Salem- 636 011, Tamil Nadu, India

^b Chemistry of Heterocycles & Natural Product Research Laboratory, Department of Chemistry, School of Advanced Sciences, Vellore Institute of Technology, Vellore, 632 014, Tamil Nadu, India

^c School of Physics, Madurai Kamaraj University, Madurai, 625021, India

^d Facultad de Ingeniería y Tecnología, Universidad San Sebastián, Bellavista 7, Santiago, 8420524, Chile

ARTICLE INFO

Keywords:

Response surface methodology
Hydrothermal
Electron migration
Pharmaceutical condemnations
Degradation intermediates

ABSTRACT

In this study, we designed and successfully prepared all solid state 2D/3D/2D rGO/Fe₂O₃/g-C₃N₄ nanocomposite by embedding 3D Fe₂O₃ nanoparticles on 2D g-C₃N₄ nanosheets to for 3D/2D Fe₂O₃/g-C₃N₄ followed by the addition of 2D rGO nanosheets via a simple hydrothermal technique with the support of response surface methodology for the first time. The formation of this unique 2D/3D/2D heterojunction leads to generate several nanochannels in their interfacial contact for high-speed photoinduced charge transfer. The considerable enhancement in photoinduced charge transportation and migration efficiency resulted in significant visible-light-driven degradation of emerging pharmaceutical condemnations. The 3D/2D Fe₂O₃/g-C₃N₄ nanocomposite was optimized by various concentrations of Fe₂O₃ in g-C₃N₄, followed by the optimization of rGO concentration in 2D/3D/2D rGO/Fe₂O₃/g-C₃N₄ nanocomposite to obtain maximum degradation efficiency. We observed that the 3% of rGO in 4% Fe₂O₃/g-C₃N₄ nanocomposite exhibited superior photocatalytic ability, nearly 22 times and 16 times higher than pristine g-C₃N₄ nanosheets towards tetracycline and ciprofloxacin degradation, respectively. The synergistic effect between 2D/3D/2D g- rGO/Fe₂O₃/g-C₃N₄ nanocomposites and the photocatalytic mechanism was well studied through various characterization techniques like XRD, FTIR, SEM-EDX-mapping, HR-TEM, UV-vis DRS, PL, XPS and EPR. In addition, the 2D/3D/2D rGO/Fe₂O₃/g-C₃N₄ nanocomposite exhibits excellent recyclability and stability, establishing a promising application in environmental remediation. This research would provide a noteworthy platform for the extensive photocatalytic properties of 2D/3D/2D heterojunction nanocomposite system with enhanced charge migration and separation.

1. Introduction

In this industrial era, the detoxification of large amounts of industrial and pharmaceutical effluents, such as organic dyes, antibiotics and pain killers from municipal water has been raised as a huge challenge. The enormous amount of pharmaceutical contaminations of fresh and municipal water resources is constantly threatening the sustainable growth of society and human health. Hence, an advanced detoxification process utilizing renewable and clean energy with low cost is needed very urgently [1–3]. As a solution for this, semiconductor

photocatalysis with an ability to utilize abundant solar energy or visible light has engrossed worldwide attention as an auspicious technique to solve a global environmental problem. While comparing with single two dimensional (2D) and three dimensional (3D) semiconductor photocatalyst, the construction of 2D/2D and 3D/2D heterojunction photocatalyst with tunable energy band structures and efficient photoexcited charge carrier separation is found to be a more promising approach to achieve high efficient photocatalytic materials [4]. The 2D/2D and 3D/2D heterojunctions will drastically enhance the coupling interface and the short photogenerated charge transfer path for

* Corresponding authors.

E-mail addresses: shanashana8@gmail.com (S. Shanavas), profpmbarasan@gmail.com (P.M. Anbarasan).

¹ Equal contributions to this work.

efficient separation of charge carriers [5]. The huge challenge in this 2D/2D and 3D/2D heterojunction photocatalyst is finding a suitable semiconductor photocatalyst with appropriate band edges and surface characteristics for the feasible synthesis of the hybrid photocatalyst. Interestingly, recent research studies have exposed an excellent photocatalytic ability of graphitic carbon nitride ($\text{g-C}_3\text{N}_4$) towards environmental purification and water splitting applications, predominantly because of its peculiar intrinsic 2D crystalline nature, high chemical stability and excellent light absorption ability with a narrow bandgap of about ~ 2.8 eV [6,7]. The $\text{g-C}_3\text{N}_4$ possess very strong reductive ability at its conduction band (CB) edge (-1.3 V) by photo-induced electrons. But the oxidation capacity ($+1.4$ V) of photoinduced holes in the valence band (VB) is very weak [8]. In addition, the recombination rate of photoexcited charge carriers is very high in $\text{g-C}_3\text{N}_4$ and this affects its photocatalytic efficiency rapidly. Therefore, considerable efforts have been taken to delay the charge carrier recombination by coupling it to other suitable 3D semiconductors and 2D rGO. Among the various photocatalytic semiconductors, Fe_2O_3 is found to be a characteristic non-toxic photocatalytic semiconductor with much narrow band gap than $\text{g-C}_3\text{N}_4$. The typical band gap energy of Fe_2O_3 is found to be ~ 2.3 eV with higher solar spectrum absorption ability (up to 600 nm) [9]. In addition, Fe_2O_3 owns several superior properties including high chemical stability, high electrical conductivity, widespread availability at earth's crust and very cheaper than other semiconductor photocatalysts. Still, the pristine Fe_2O_3 possesses an average photocatalytic ability due to high e^- - h^+ pair recombination rate [10–12]. In previous investigations, it has been reported that the development of Fe_2O_3 nanoparticles instead of bulk Fe_2O_3 can enhance its photocatalytic ability largely [13]. Hence it is expected that the embodiment of 3D Fe_2O_3 nanoparticles on the surface of 2D $\text{g-C}_3\text{N}_4$ to form 3D/2D heterojunction can enhance their photocatalytic ability. The formation of 3D/2D $\text{Fe}_2\text{O}_3/\text{g-C}_3\text{N}_4$ nanostructure is expected to overcome some intrinsic disadvantages of 2D $\text{g-C}_3\text{N}_4$ like lower e^- - h^+ pair separation efficiency and limited visible-light absorption ability [10,13]. Up till now, the synthesis of $\text{g-C}_3\text{N}_4$ with other photocatalytic semiconductors has been carried out using conventional hydrothermal methods through the simple procedure of mixing two pristine photocatalysts together [10,14,15]. But the effect of pristine 3D semiconductor metal oxides embedment on 2D $\text{g-C}_3\text{N}_4$ nanosheets was rarely exploited. Xin Liu et al., has reported the photocatalytic ability of $\text{g-C}_3\text{N}_4$ decorated with ultrafine Fe_2O_3 under visible-light irradiation, but still, the photocatalytic ability of $\text{Fe}_2\text{O}_3/\text{g-C}_3\text{N}_4$ is not up to par for commercial utilization [7]. To overcome this lag, another 2D electron trapping material can be used to restrict the $\text{e}-\text{h}^+$ pair recombination which will consequently enhance the photocatalytic ability. The formation of 2D/3D/2D photocatalytic nanostructures will increase charge transporting nanochannels more efficiently.

When compared with other 2D nanostructures, rGO exhibits excellent photocatalytic performance when it is composed of other semiconductor photocatalytic materials. Especially, 2D/2D and 2D/3D interfacial contact between rGO and other photocatalytic semiconductors have been accepted as a prime factor for sufficient trapping or transportation of photoexcited charge carriers [16,17]. Furthermore, the unique 2D structure of rGO contains several functional groups on its surface and it will act as active absorption sites of pharmaceutical molecules. The rich oxygen functional groups on the 2D surface of rGO enhance the ability of rGO to interact with other organic/inorganic compounds to form hybrid nanocomposites [1,18]. Based on the above discussion, the 2D/3D/2D heterojunction is the desired heterojunction that we are looking for. The photoexcited charge carrier migration distance plays a major role in the recombination of $\text{e}-\text{h}^+$ pairs occur rapidly and it affects the active species production rate while the migration distance is higher. The unique advantage of 2D/3D/2D heterojunction is the shortening of photoexcited charge carrier migration distance for effective suppression of $\text{e}-\text{h}^+$ pair recombination [5]. Hence, the construction of 2D/3D/2D type heterojunction can create

numerous high-speed photoinduced charge transfer nanochannels in rGO/ $\text{Fe}_2\text{O}_3/\text{g-C}_3\text{N}_4$ nanocomposite. The expected photoinduced electron migration route is from Fe_2O_3 to the intimate heterojunction interface between another couple of 2D nanosheets (rGO and $\text{g-C}_3\text{N}_4$). The photoinduced electron migration process is similar to the real-life freeways and it will result in enhanced photoinduced charge transfer and separation efficiency for effective photocatalytic activity [6,19,20]. Herein, as an eager to study the photocatalytic pharmaceutical molecule degradation ability of unique 2D/3D/2D heterojunction, we design and construct a ternary nanocomposite structure of rGO/ $\text{Fe}_2\text{O}_3/\text{g-C}_3\text{N}_4$ photocatalyst with the unique faster-photoexcited charge transfer nanochannels through the simple hydrothermal process using response surface methodology. The synthesized 2D/3D/2D-rGO/ $\text{Fe}_2\text{O}_3/\text{g-C}_3\text{N}_4$ nanocomposite is studied with various characterization techniques such as XRD, FTIR, SEM, TEM, UV-vis DRS, EPR and XPS to understand the intrinsic link between 2D/3D/2D geometry structure and it exhibits a remarkable photocatalytic degradation ability towards pharmaceutical molecules (Tetracycline and ciprofloxacin).

2. Experimental section

2.1. Materials

Ferric nitrate ($\text{Fe}(\text{NO}_3)_3$), melamine, graphite flakes, potassium permanganate (KMnO_4), sulfuric acid (H_2SO_4), methanol, ethanol, ciprofloxacin (CP), Tetracycline (TC), sodium hydroxide (NaOH), sulfuric acid (H_2SO_4), sodium nitrate (NaNO_3), terephthalic acid (TA), isopropyl alcohol (IPA), p-benzoquinone (BQ) and triethanolamine (TEOA). All reagents were purchased from Merck Chemical Co., with an analytical grade and used without further purification.

2.2. Preparation of 3D/2D- $\text{Fe}_2\text{O}_3\text{-C}_3\text{N}_4$ and 2D/3D/2D-rGO/ $\text{Fe}_2\text{O}_3/\text{g-C}_3\text{N}_4$ nanosheets

A single step embedment approach was used to synthesis $\text{Fe}_2\text{O}_3/\text{g-C}_3\text{N}_4$ nanosheets. In this method of synthesis, the precursor solution having stoichiometric ratio of $\text{Fe}_{(x)}\text{-melamine}_{(100-x)}$ was prepared by dissolving x mol% of ferric nitrate ($\text{Fe}(\text{NO}_3)_3$) and $100-x$ mol% of melamine in 100 ml of methanol:DI (1:1) and kept under stirring for 5 h to obtain homogeneous solution. Then the mixture was kept in a hot air oven at 80°C for 8 h to get the reddish yellow powder and it was well grounded until a fine powder is formed. The ground fine powder was transferred to the crucible and calcined using muffle furnace at 550°C for 5 h in air atmosphere. The calcined material was well grounded again to attain reddish yellow $\text{Fe}_2\text{O}_3/\text{g-C}_3\text{N}_4$ (FC) nanosheets. The similar single step procedure was carried out for the preparation of other Fe_2O_3 embedded C_3N_4 nanosheets with different molar ration ($x = 0.25, 0.5, 1, 2, 4$ and 6 mol%) of Fe_2O_3 precursors. The obtained products were named as 0.25FC, 0.5FC, 1FC, 2FC, 4FC and 6FC. At the same time, the pure $\text{g-C}_3\text{N}_4$ nanosheets were prepared without the addition of Fe precursors.

2.3. The RSM optimization of the preparation of the 3D/2D- $\text{Fe}_2\text{O}_3\text{-C}_3\text{N}_4$ and 2D/3D/2D-rGO/ $\text{Fe}_2\text{O}_3/\text{g-C}_3\text{N}_4$ nanosheets

To get a proper synthesis of the 3D/2D- $\text{Fe}_2\text{O}_3\text{-C}_3\text{N}_4$ & 2D/3D/2D-rGO/ $\text{Fe}_2\text{O}_3/\text{g-C}_3\text{N}_4$ nanosheets using RSM methodology. Correspondingly, there are three levels, which were used by the 25-run BBD quadratic model. Accordingly, the effects of three operating parameters including Reaction time (X_1), Reaction temperature (X_2) and molar concentration (X_3) on the preparation of the nanosheets efficiency were investigated in this study. The corresponding range of independent parameters had been determined based on the preliminary experiments, as presented in Table 1.

After getting the results were correlated into the quadratic polynomial equation $Y = \beta_0 + \sum_{i=1}^n \beta_i x_i + \sum_{i=1}^n \beta_{ii} x_i^2 + \sum_{i=1}^n \sum_{j>1}^n \beta_{ij} x_i x_j$

Table 1
Experimental range and levels of the independent variables.

Variables	Units	Level		
Reaction time	Hours	-1	0	+1
		7	8	9
Reaction Temperature	°C	70	80	90
Molar concentration	mol %	2	4	6

$\Sigma X_i Y_j$. Here, Y denotes predicted response, n denotes number of experiments, the β_0 , β_1 , β_{ii} , and β_{ij} are regression coefficients for the constant, linear, quadratic and interaction coefficients, respectively and X_i and X_j are the coded independent factors [21].

2.4. Preparation of rGO substituted Fe_2O_3 - C_3N_4 nanosheets

The preparation of (y)rGO/ Fe_2O_3 /g-C₃N₄ (FCG) nanostructures was carried out by adding specific amounts ($y = 1, 2, 3, 4$ and 5 mass%) of rGO sheets with 4FC nanostructures in 50 ml of DI water under constant stirring for 3 h followed by hydrothermal treatment at 200 °C for 12 h. The graphical representation of FCG is shown in Fig. 1. Initially, GO was prepared by the modified hummers method and then the as-prepared GO is transferred to autoclave followed by hydrothermal treatment at 140 °C for 5 h to prepare rGO sheets [22].

2.5. Characterization techniques

XRD patterns of as-synthesized photocatalyst were recorded using Rigaku Miniflex X-ray diffractometer equipped with Cu K α ($\lambda = 1.54 \text{ \AA}$) radiation operating at 40 kV with 30 mA. Fourier transformed infrared (FT-IR) spectra were recorded through Brucker Tensor 27 FT-IR spectrophotometer in the range between 4000 cm⁻¹ and 400 cm⁻¹ at KBr phase. X-ray photoelectron spectroscopy (XPS) analysis was conducted through Krotas analytical Instrument, ESCA 3400, with Dual Mg/Al anodes and operating voltage at 12 kV with 25 mA under ultra-high vacuum condition. Field emission Scanning electron microscope (FE-SEM) images and energy dispersive X-rays spectroscopy (EDS) graph was observed using (Hitachi, S-4800). High-resolution transmission electron microscopy (HR-TEM) was carried out using Jeol/JEM 2100 high-resolution transmission electron microscope operating at 200 kV. Photoluminescence (PL) spectra were measured at room temperature by Perkin Elmer LS-45 spectrophotometer. UV-vis Diffuse Reflectance Spectra (UV-vis-DRS) were recorded by SHIMADZU-UV 1800 spectrometer in the wavelength range between 200 nm and 800 nm.

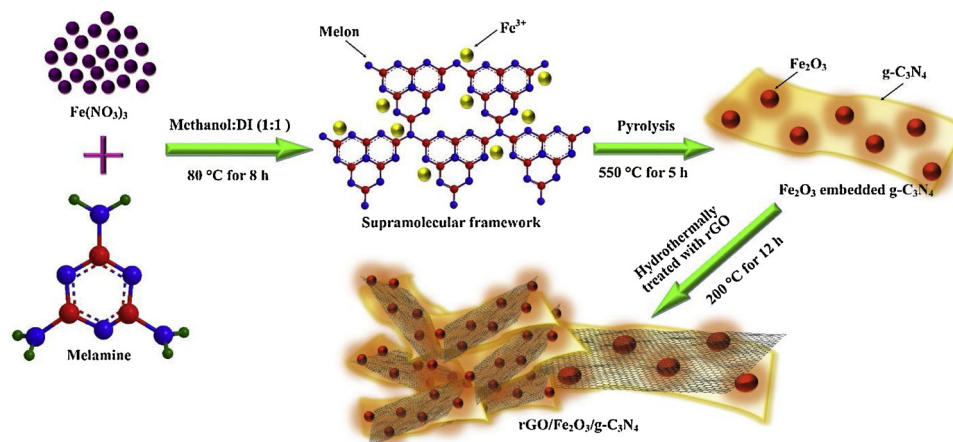


Fig. 1. Schematic illustration of the synthesis of 2D/3D/2D-rGO/ Fe_2O_3 -g-C₃N₄ nanocomposite.

2.6. Photocatalytic examination

The photocatalytic degradation ability of as-synthesized nanostructures was examined by degrading TC and CP Pharmaceutical molecules as model carcinogens under visible light irradiation by 500 W halogen lamp equipped with UV filter. In the typical photocatalytic reaction solution, 50 mg of the photocatalyst was well dispersed in 100 ml of 20 mg/l carcinogen solution and the pH of the reaction solution is maintained at 7. Before visible light irradiation, the photocatalytic reaction solution was well stirred in the dark for 30 min to obtain adsorption-desorption equilibrium with the catalytic surface. Then the reaction solution was irradiated under the halogen lamp at 100 mm distance from the light source. At the regular periodic intervals of 15 min, 4 ml of the reaction solution was collected and well centrifuged in order to remove dispersed catalyst and the supernatant was characterized by UV-vis spectrophotometer to determine the temporal concentration of carcinogen in the reaction solution. The photocatalytic degradation ability of as-prepared nanostructures was also examined in different initial parameters like catalyst dosage (0.25 g to 1.5 g), carcinogen concentration (10 mg/l to 40 mg/l) and pH (2–12) of photocatalytic solution. The photocatalytic degradation rate constant of as-synthesized nanosheets was calculated by using the degradation kinetics of TC and CP. The photocatalytic stability and recyclability of as-synthesized nanostructures were analyzed by cyclic experiments of carcinogen degradation.

2.7. Trapping experiment and hydroxyl radical estimation

The generation of reactive species and predominant radical responsible for carcinogen degradation was found through a trapping experiment. In a trapping experiment, the utilization rate of hydroxyl radical (·OH), Superoxide radical (O₂^{·-}), and holes (h⁺) towards carcinogen degradation were investigated by adding 1 mmol/L of respective quenching agents like IPA (for ·OH quenching), BQ (for O₂^{·-} quenching) and TEOA (for h⁺ quenching) in typical photocatalytic reaction solution [23,24]. The hydroxyl radical production efficiency of as-synthesized nanosheets was determined through PL spectroscopic analysis using TA as a probe molecule in a typical photocatalytic experiment in the absence of carcinogens. In this reaction, the ·OH radicals generated by the photocatalyst will react with TA to produce fluorescent molecule 2-hydroxyterephthalic acid (HTA) which is detected through PL spectroscopy. The intensity of HTA molecules gives evidence of ·OH radical production [25].

3. Results and discussion

3.1. RSM Design for the preparation of the 3D/2D- $\text{Fe}_2\text{O}_3\text{-C}_3\text{N}_4$ and 2D/3D/2D-rGO/ $\text{Fe}_2\text{O}_3\text{/g-C}_3\text{N}_4$ nanosheets

Response surface methodology (RSM) is one of the best methodologies for the optimizations of the various parameters. Here we are mainly focused on the reaction time, reaction temperature and molar ratio of the Fe_2O_3 precursors. The above three parameters are taken for the study being investigated for five different parameters like Degrees of freedom, the sum of squares, Mean square, *F*- value and *p*-value. Every point analyzed from higher parameter range to lower range. The reaction time is taken from minimum 7 h to 9 h as well as the temperature minimum of 70 to 90 °C and molar ratio also given that range 2 to 6 mol%. From this parameter, we changed the ratios of the preparation of the 2D/3D/2D-rGO/ $\text{Fe}_2\text{O}_3\text{/g-C}_3\text{N}_4$ nanosheets, for that we absorbed various the absorption maximum for thought regarding this optimization study. A maximum absorption response was appeared using RSM.

The model developed to fit a quadratic equation is $Y = 0.781 + 0.0619 \text{ (Time)} + 0.0957 \text{ (Temp)} + 0.0846 \text{ (Molar ratio)}$, the experiment results were analyzed using the interaction between each independent variable shown in the Table 2.

The above regression model explains perfectly the experimental range studied, as can be seen from the comparison of the graphical representation of observed versus predicted values (Fig. S1). The observed absorption maximum varied between in all ratios and the model prediction matched these observational results satisfactorily. The results of the analysis of variance (ANOVA) for absorption maximum 'Y' were summarized in Table 3. The analysis showed that the *p*-value (less than 0.05) as a statistic test indicated that the model terms are significant. In this case time, temperature and are significant model terms. The parameter having the most significant effect on absorption maximum, the *p*-value is the smallest in value for all conditions. The optimum condition for maximum absorption is timed at 8 h and the temp in 80 °C, the molar ratio is 4 mol % from the predicted model. At this optimum condition, the observed absorption maximum is 1.02 experimentally.

Table 2
The BBD matrix of Time, Temperature and Molar ratio.

Run	Time	Temp	Molar ratio	Absorption Maximum
1	-1	-1	-1	0.61
2	1	-1	-1	0.55
3	-1	0	-1	0.53
4	0	0	-1	0.67
5	1	0	-1	0.72
6	-1	1	-1	0.82
7	0	1	-1	0.78
8	1	1	-1	0.84
9	-1	-1	0	0.65
10	0	-1	0	0.61
11	1	-1	0	0.76
12	-1	0	0	0.75
13	0	0	0	0.92
14	1	0	0	1.06
15	-1	1	0	0.83
16	0	1	0	0.95
17	1	1	0	0.84
18	-1	-1	1	0.63
19	0	-1	1	0.82
20	1	-1	1	0.84
21	-1	0	1	0.79
22	0	0	1	0.87
23	1	0	1	0.96
24	-1	1	1	0.83
25	0	1	1	0.88

Table 3
Analysis of Variance for absorption maximum.

Source	DF	Seq SS	Sum of Sq	Mean Sq	F	P
Regression	9	0.316219	0.316219	0.035135	5.92	0.001
Linear	3	0.271169	0.250390	0.083463	14.06	0.000
Square	3	0.023949	0.024593	0.008198	1.38	0.287
Interaction	3	0.021102	0.021102	0.007034	1.18	0.349
Residual Error	15	0.089045	0.089045	0.005936		
Total	24	0.405264				

3.1.1. Surface plots and contour plots of optimization

The 3D response surface plots were used for the analysis of the interactions. From Fig. 2a, it has been observed that the absorption maximum for nanosheets increases with increase in temperature and decreases with further increase in temperature. Fig. 2b shows that the absorption maximum increases with increase in molar ratio and decreases with further increase in ratio because of the rate of reaction. Fig. 2c and d shows contour plots for the absorption maximum ratio corresponding temperature, time and molar ratio. The contour plots are the graphical representation of the regression equation used to visualize the relationship between the response and experimental levels of each factor. The absorption maximum is the maximum in the molar ratio range 4–6 mol% as shown in Fig. 2c and from Fig. 2d, it is shown that the absorption maximum is the maximum in the temperature range 80–90 °C.

3.2. XRD analysis

The XRD analysis of the as-prepared pristine $\text{g-C}_3\text{N}_4$, pristine Fe_2O_3 , $\text{Fe}_2\text{O}_3\text{/g-C}_3\text{N}_4$ and rGO/ $\text{Fe}_2\text{O}_3\text{/g-C}_3\text{N}_4$ nanostructures were shown in Fig. 3a and Fig. S2. The XRD pattern of $\text{g-C}_3\text{N}_4$ nanostructures shows a strong characteristic diffraction peak at $2\theta = 27.7$ is due to typical interlayer spaced stacking interactions between conjugated carbon melon systems and it corresponds to (002) crystal plane of the $\text{g-C}_3\text{N}_4$ nanostructure. The less intense peak at around 13.6 corresponds to (100) plane, formed due to the in-plane repetitive hole to hole packing separation in continuous tri-s-triazine motif [3,26]. After doping Fe_2O_3 , with $\text{g-C}_3\text{N}_4$ structure the characteristic peaks of Fe_2O_3 nanoparticles were present at $2\theta = 33.02$, 35.58, 38.42, 49.42, 53.98, 62.48 and 64.01 corresponds to (104), (110), (113), (024), (116), (214) and (300) crystal planes agrees to rhombohedral phase (JCPDS: 89-8104) shows the formation of Fe_2O_3 doped $\text{g-C}_3\text{N}_4$ nanostructures [27,28]. The similar rhombohedral phase of Fe_2O_3 has observed in all doping concentrations confirms the formation of Fe_2O_3 , with uniform phase in a series of $\text{Fe}_2\text{O}_3\text{/g-C}_3\text{N}_4$ nanostructures (Fig. 3a). The XRD graphs of Fe_2O_3 doped $\text{g-C}_3\text{N}_4$ shows a little peak shift towards lower diffraction angle with change in peak width, this alteration in (002) peak shows the interaction between Fe_2O_3 and carbon melon units of $\text{g-C}_3\text{N}_4$ [27]. The peak shift towards lower diffraction angle is can be attributed to the interlamellar spacing of $\text{Fe}_2\text{O}_3\text{/g-C}_3\text{N}_4$ nanostructures. In the case of 0.25FC, 0.5FC and 1FC none of the Fe_2O_3 XRD peaks were present and this is due to the lower doping concentration. While increasing the dopant concentration the intensity of Fe_2O_3 XRD peaks are also gradually increasing, but at 6% of Fe_2O_3 concentration the intensity of Fe_2O_3 XRD peak is decreasing, it is due to the creation of oxygen vacancies at higher doping concentrations [29,30]. The XRD diffractographs series of rGO substituted 4FC nanostructures were shown in Fig. 3b. The formation of rGO/ $\text{Fe}_2\text{O}_3\text{/g-C}_3\text{N}_4$ nanostructure was confirmed by the presence of characteristic rGO peak at $2\theta = 26.4$ corresponds to its (002) plane. Interestingly, after the addition of rGO sheets with 4FC nanostructure, the diffraction peak width becomes broader with weaker peak intensities. In addition to that, the peak shifting of both $\text{g-C}_3\text{N}_4$ and Fe_2O_3 nanostructures towards the lower diffraction angle was also observed. The change in diffraction peak properties is due to the guest-host interaction between rGO sheets and 4FC

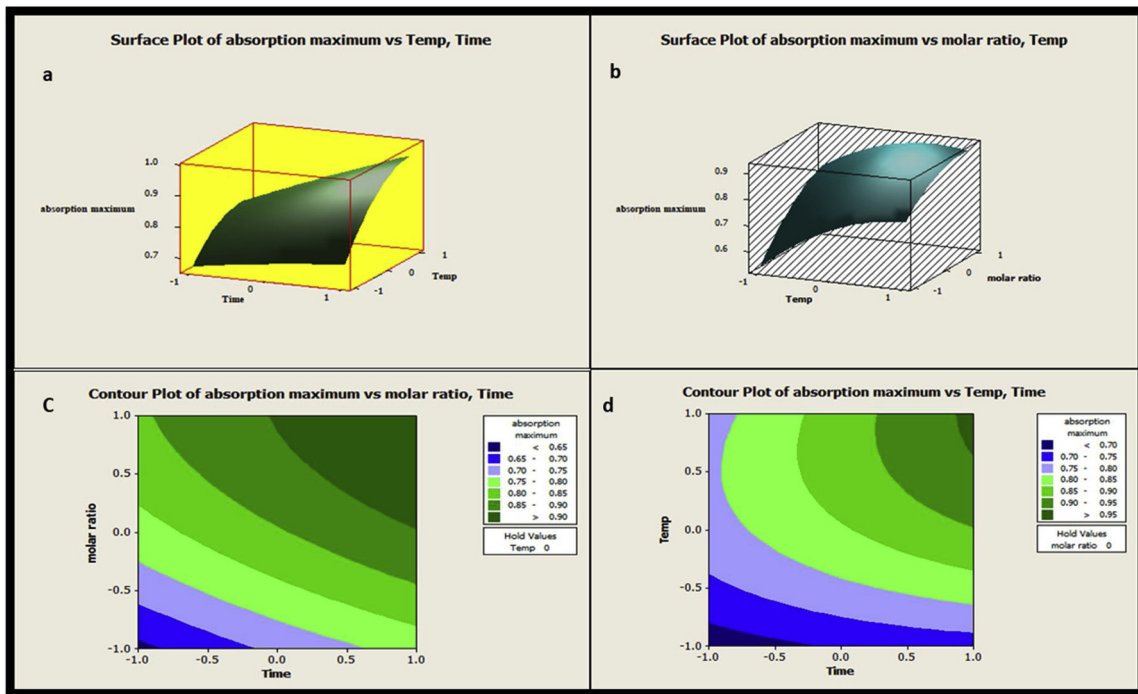


Fig. 2. (a) Response surface plot showing absorption maximum Vs reaction temperature, time (b) response surface plot showing absorption maximum Vs reaction temperature, molar ratio (c) contour plot showing absorption maximum Vs reaction temperature, time, (d) contour plot showing absorption maximum Vs reaction temperature, the molar ratio.

nanostructure with the polymeric condensation inhabitation by higher rGO concentration [16]. The d-spacing of Fe_2O_3 is calculated to be 0.25 nm from its intense peak centered at $2\theta = 33.2^\circ$ by using Bragg's law.

3.3. Functional group analysis using FT-IR and structural analysis using Raman

The surface characteristics and functional group investigation of as-synthesized pristine $\text{g-C}_3\text{N}_4$, Fe_2O_3 , 3D/2D-4FC and 2D/3D/2D-4FC3G nanostructures were carried out using FT-IR spectroscopic analysis and the obtained FT-IR transmission spectrum is shown in Fig. S3a. The photocatalytic degradation of organic pharmaceutical condemnations is highly depended on the interaction between pharmaceutical molecules and photocatalytic surface. The carboxyl functional groups on the surface of photocatalytic materials play a major role in the pharmaceutical molecule-catalyst interaction. The FT-IR spectrograph of pristine $\text{g-C}_3\text{N}_4$ nanosheets shows several strong transmission peaks between 1200 cm^{-1} - 1650 cm^{-1} and they corresponds to typical CN

heterocycle stretching modes and strong transmission peak at 805 cm^{-1} attributes to the breathing vibrational modes of triazine units in the cyclic $\text{g-C}_3\text{N}_4$ structure. The presence of uncondensed fatal $-\text{NH}_2$ / $=\text{NH}$ groups at the defect sites of the aromatic ring in the cyclic $\text{g-C}_3\text{N}_4$ structure were identified by a broad transmission band between 2850 cm^{-1} and 3375 cm^{-1} [10,31,32]. The pristine Fe_2O_3 nanostructure shows the strong transmission peak at 500 cm^{-1} and it is attributed to the presence of Fe–O–Fe (metal–oxygen) bonding. The FT-IR spectra of bare GO and rGO sheets were shown in Fig. S3b. The FT-IR transmission spectral bands at 3433 cm^{-1} and 1620 cm^{-1} were attributed to the stretching bonds of hydroxyl ($-\text{OH}$) groups and $-\text{OH}$ bending or in-plane vibrations of sp^2 -hybridized C=C bond, respectively. The FT-IR transmission peaks at 2820 cm^{-1} are due to the C–H aliphatic stretching and the peaks at 1724 cm^{-1} are observed due to the carboxyl ($-\text{C=O}$) group. The obtained peak at 1221 cm^{-1} is observed due to the stretching vibration of ($-\text{C–OH}$). In case of the FT-IR spectrum of bare rGO, some of the oxygen-containing transmission peaks were decreased and even disappeared. This revealing the removal of oxygen-containing functional groups after thermal reduction of GO. The decrement in the

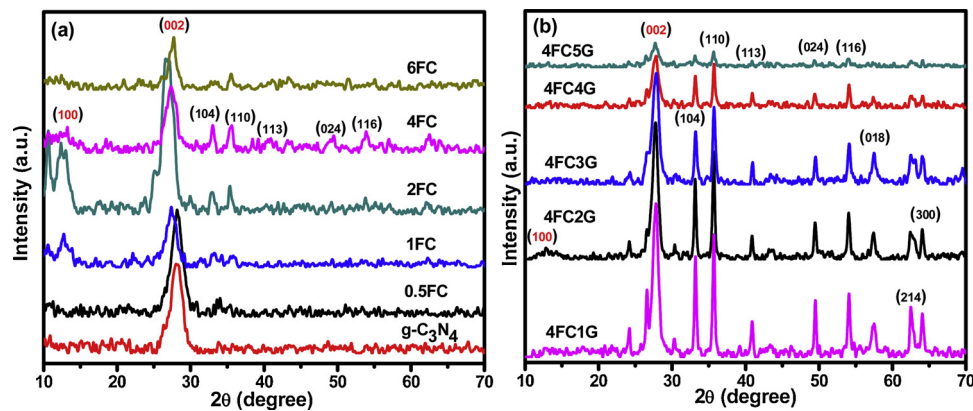


Fig. 3. XRD patterns of as-prepared (a) pristine $\text{g-C}_3\text{N}_4$, pristine Fe_2O_3 , binary $\text{Fe}_2\text{O}_3/\text{g-C}_3\text{N}_4$ and (b) rGO/ $\text{Fe}_2\text{O}_3/\text{g-C}_3\text{N}_4$ ternary nanocomposite.

intensity of $-\text{OH}$ peak was observed after thermal reduction of GO to form rGO. The stretching vibrational peak at 1221 cm^{-1} was also almost disappeared confirms the decrement in the oxygen group. The above-obtained FT-IR results suggest the successful reduction of GO to rGO after thermal treatment. The presence of transmission peaks corresponding to $\text{g-C}_3\text{N}_4$ nanosheets can be found in both 3D/2D-4FC and 2D/3D/2D-4FC3G nanostructures confirm the formation of well-composed nanostructures [33]. The FT-IR transmission spectrum of 4FC3G ternary nanocomposite shows skeletal vibrational transmission band of aromatic $\text{C}=\text{C}$ and $\text{C}-\text{O}$ stretching bands at 1630 cm^{-1} and 1250 cm^{-1} , respectively [22]. The presence of $\text{Fe}-\text{O}-\text{Fe}$ (metal-oxygen) bonding and transmission bands of $\text{g-C}_3\text{N}_4$ was also observed in the FT-IR transmission spectra of 4FC3G nanocomposites and it confirms the successful incorporation of both Fe_2O_3 and $\text{g-C}_3\text{N}_4$ on rGO nanosheets [17]. A wide FT-IR peak observed at 3300 cm^{-1} - 3500 cm^{-1} corresponds to the stretching mode of hydroxyl groups on the catalytic surface. The formation of such $-\text{OH}$ group is due to the presence of physically absorbed H_2O molecules on the catalytic surface from the atmosphere.

The successful reduction of GO into rGO is further confirmed using Raman analysis shown in Fig. S3c. The Raman peaks observed at 1345 cm^{-1} and 1580 cm^{-1} of GO is due to the D band and G band, respectively. The D band and G band of rGO are observed at 1325 cm^{-1} and 1576 cm^{-1} , respectively. The D band is due to the $\text{A}1\text{g}$ defect mediated breathing mode and G band is owing to the $\text{E}2\text{g}$ mode first order scattering. The ID/IG ratio of GO is found to be 0.84 and the ID/IG ratio of rGO is increased as 0.85. Thus increment in ID/IG ratio is credited to the formation of sp^2 domains during the thermal reduction of GO into rGO. On another hand, the peak shift observed towards lower wavenumber of G band from 1583 cm^{-1} (GO) to 1578 cm^{-1} (rGO) after thermal reduction process confirms the formation of more domains of graphene.

3.4. Chemical state analysis

In order to elucidate the surface chemical composition and binding states of the elements present in 4FC3G, the XPS analysis was performed and the survey scan XPS spectra of respective nanocomposite are shown in Fig. 4a. The strong peaks appeared at 284.4 eV , 398.4 eV , 530.8 eV and 710.7 eV indicating the presence of elemental C, N, O and Fe respectively in the 4FC3G nanocomposite. The C-1s high-resolution XPS spectrum is shown in Fig. 4b. The strong peak observed at 284.4 eV ascribes to the binding of sp^2 -hybridized carbon atoms of rGO and the highest binding energy peaks reveal the presence of oxygenated carbon atomic species like COH , COOH and $\text{C}=\text{O}$ in ternary nanocomposite [16,17,32]. The presence of such oxygenated groups serves as reaction sites as well as interaction sites with $\text{g-C}_3\text{N}_4$ and Fe_2O_3 nanostructures. The FTIR analysis and elemental mapping analysis has also confirmed the presence of rich oxygen sites. The broad peak at 286.6 eV corresponds to the sp^2 -hybridized atomic carbon present inside the aromatic structure with three nitrogen atoms adjacent to carbon atoms in $\text{g-C}_3\text{N}_4$ lattice [26]. The N-1 s XPS spectra (Fig. S4) of pristine $\text{g-C}_3\text{N}_4$ projects two typical peaks at 398.6 eV and 400.9 eV . The high intense peak at 398.6 eV was attributed to aromatic N with sp^2 -hybridization bonded with $\text{C}(\text{N}-\text{C}=\text{N})$ in the triazine rings of graphitic carbon. The N 1s spectra of 4FCG are shown in Fig. 4c, the high intense peak of pyridine N in 4FC3G at 398.4 eV and the peak at 400.7 shows the decrement in the binding energy by 0.2 eV when compared with the pristine $\text{g-C}_3\text{N}_4$. The peak shift reflects the interfacial interaction between Fe_2O_3 and $\text{g-C}_3\text{N}_4$ nanosheets [1,7,34]. The peaks at 710.7 eV and 724.3 eV of Fe-2p high resolution XPS spectra (Fig. 4d) corresponds to $\text{Fe}-2\text{p}_{3/2}$ and $\text{Fe}-2\text{p}_{1/2}$, respectively. This shows the Fe^{3+} oxidation state in the 4FC3G nanocomposite. In addition, the $\text{Fe}-2\text{p}_{3/2}$ and $\text{Fe}-2\text{p}_{1/2}$ spin-orbit splitting are calculated to be 13.6 eV , it further confirms the formation of Fe^{3+} ions in the 4FC3G nanocomposite. The peak at 710.7 eV of $\text{Fe}-2\text{p}_{3/2}$ shows the well stabilized Fe species in the electron-rich graphitic

carbon structure through Fe-N bonds. It confirms the formation of Fe-N coordinate bonds with Fe^{3+} atoms connected to the N atom [15,35,36]. The XPS spectrum of O-1 s shown in Fig. 4e displays a single high intense peak at 530.8 eV corresponds to an oxygen atom bonded with Fe metal ions confirms the formation of Fe_2O_3 in the 4FC3G nanostructure. The obtained results were also in good agreement with XRD, FTIR and elemental mapping characterization of the as-prepared 4FC3G nanostructure.

3.5. Morphological and elemental characterization

The detailed morphological properties of as-prepared pristine $\text{g-C}_3\text{N}_4$, 3D/2D-4FC and 2D/3D/2D-4FC3G nanostructures were revealed through HR-TEM and shown in Fig. 5. Fig. 5a shows the arrangement of the dense curved sheet-like pristine 2D- $\text{g-C}_3\text{N}_4$. The formation of such highly dense thinner $\text{g-C}_3\text{N}_4$ nanosheets is due to the thermal oxidation exfoliation at $550\text{ }^\circ\text{C}$ of bulk $\text{g-C}_3\text{N}_4$. The two-dimensional sheet-like $\text{g-C}_3\text{N}_4$ can efficiently restrain the recombination of photoinduced charge carriers by shortening its vertical movement distance [5]. The HR-TEM images of pristine Fe_2O_3 nanoparticles was shown in Fig. S5. The obtained results show the formation of 3D Fe_2O_3 nanoparticles with irregular spherical in shape. The average particle size of Fe_2O_3 nanoparticles was found to be 35 nm which confirms the 3D nature of Fe_2O_3 nanoparticles. The lattice spacing with a distance of 0.25 nm was observed from Fig. S5c. and it is well matched with the result obtained from XRD analysis using its intense XRD peak centered at $2\theta = 33.2^\circ$ calculated by Bragg's law. The good embedding of Fe_2O_3 nanoparticle in the $\text{g-C}_3\text{N}_4$ matrix was clearly visible in 4FC nanostructure shown in Fig. 5b, this confirms the formation of tightly embedded $\text{Fe}_2\text{O}_3/\text{g-C}_3\text{N}_4$ nanostructures. The interaction between metal oxides and $\text{g-C}_3\text{N}_4$ were highly increased by the embedding metal oxides in $\text{g-C}_3\text{N}_4$ nanostructures than the deposition of metal oxides in the surface of $\text{g-C}_3\text{N}_4$. The embedment of Fe_2O_3 nanostructures in $\text{g-C}_3\text{N}_4$ nanosheets will effectively increase the photoexcited charge carrier transportation from Fe_2O_3 to $\text{g-C}_3\text{N}_4$ and vice-versa. The improved photoexcited charge carrier transportation will lead a way for the effective decrement in e^-h^+ pair recombination [17,33]. Fig. 5c shows the formation of 4FC3G nanocomposite with Fe_2O_3 nanoparticle packed between $\text{g-C}_3\text{N}_4$ and rGO nanosheets. Such close contact between Fe_2O_3 nanoparticle embedded $\text{g-C}_3\text{N}_4$ with rGO will further trap the excited electrons from Fe_2O_3 results with the more trapping of photoexcited charge carriers. The formation of such closely stacked 2D structures will sufficiently interact with each other in a face-to-face way results in with the formation of the huge effective heterojunction interface [4,5]. In Fig. 5c, the $\text{g-C}_3\text{N}_4$ and rGO sheets can be identified by their contrast as the darker sheets are due to rGO and the lighter one is due to $\text{g-C}_3\text{N}_4$ [16]. The FE-SEM images of 4FC3G nanostructure shown in Fig. 6a-c displays the formation of a well aggregated large number of 4FC3G nanosheets combines to form a micro-sized bundle it shows the good composition of ternary composites. Fig. 6c clearly shows a large number of leaf-like 4FC3G arrangement. The formation of such tight interaction between nanosheets highly promotes the e^-h^+ charge separation and transformation [17]. The good embedment of Fe_2O_3 nanoparticles with $\text{g-C}_3\text{N}_4$ matrix and rGO is further supported by XPS analysis of 4FC3G composite by detecting the very weak signals of Fe. In further, the purity and the elemental distribution in 4FC3G nanostructure were studied by energy-dispersive X-ray spectroscopy (EDX) and elemental mapping for C, N, O and Fe were shown in Fig. 6d-i. The EDX graph shown in Fig. 6d confirms the presence of C, N, O and Fe in 4FC3G nanocomposite and no other elements were detected in EDX proves the highly pure 4FC3G. The C, N, O and Fe were displayed in various colors to recognize their positions in the nanocomposite. The higher concentration of dotted spots on an elemental map declares the concentration of respective elements in the nanocomposite. From Fig. 6f,g the uniform and denser distribution of C and N were clearly observed and it resembles the presence of $\text{g-C}_3\text{N}_4$. The concentration of C is

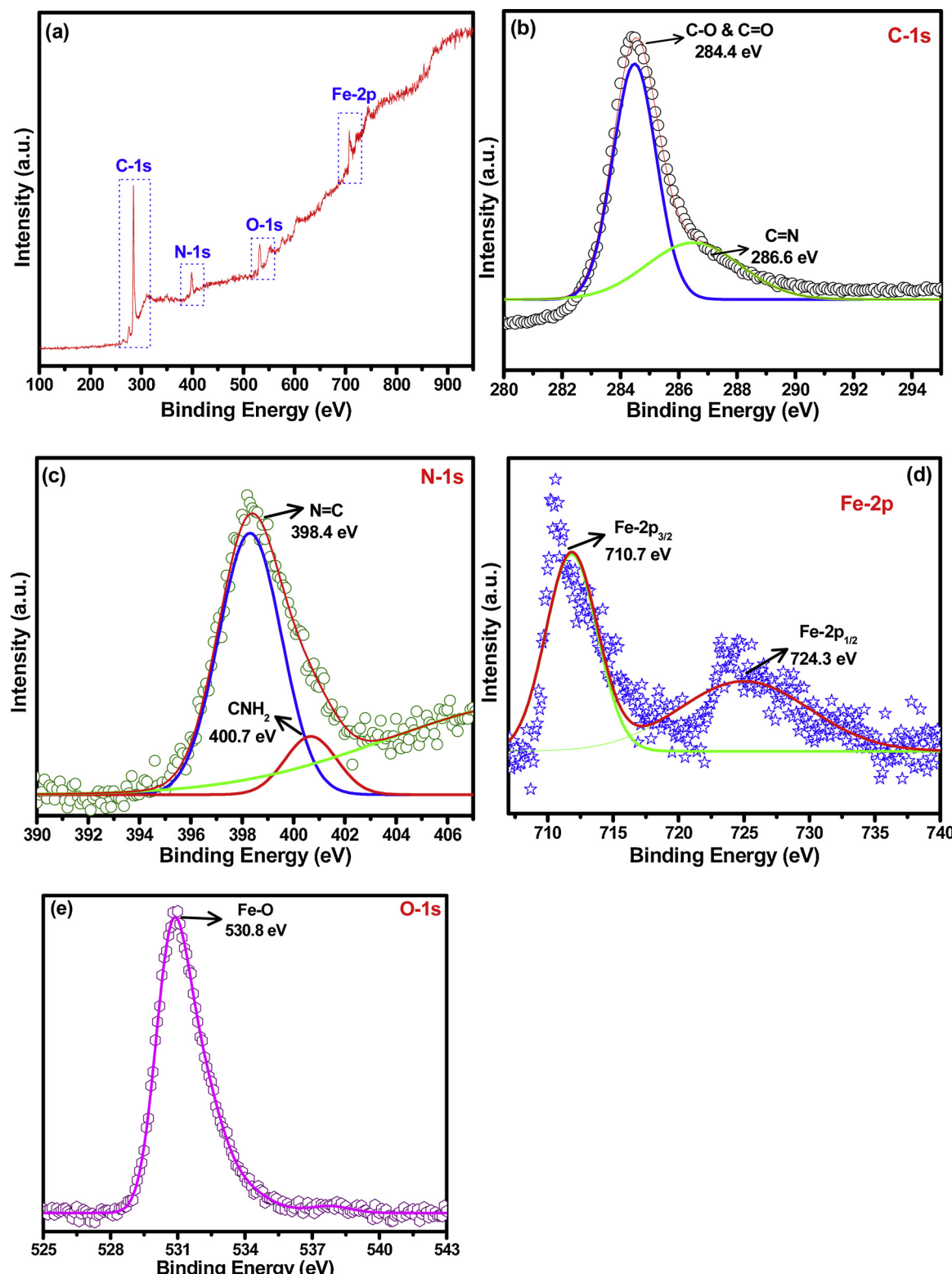


Fig. 4. XPS spectra of as-prepared 4FC3G ternary nanocomposite: (a) survey spectra (b) C-1 s spectra (c) N-1 s spectra (d) Fe-2p spectra and (e) O-1 s spectra.

comparatively higher than N and it is due to the presence of rGO. The lower concentration of O in 4FC3G further confirms the successful reduction of GO into rGO. The discrete distribution of Fe suggesting the good embedment of Fe₂O₃ nanoparticles in g-C₃N₄ and rGO. The lower intensity in Fe is also due to the screening of sheet-like g-C₃N₄ and rGO. The above results confirmed the successful preparation of 2D/3D/2D-4FC3G ternary nanocomposite.

3.6. Optical characterization

The enhanced light absorption ability is the prime factor to be an efficient photocatalyst and it is closely linked to the electronic band structures of photocatalytic materials. The optical absorption properties of as-prepared series of pristine g-C₃N₄, FC and FCG nanostructures were analyzed by UV-vis diffuse reflectance (UV-vis-DRS)

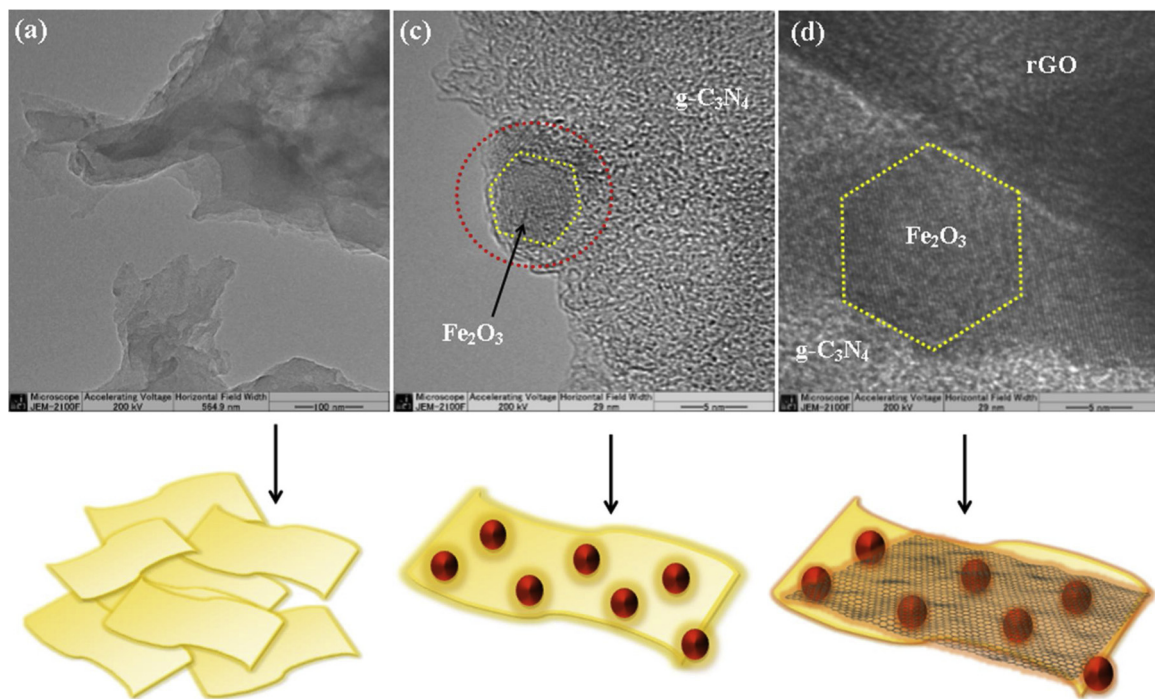


Fig. 5. HR-TEM images: (a) pristine $\text{g-C}_3\text{N}_4$ (b) 3D/2D-4FC binary and (c) 2D/3D/2D-4FC3G ternary nanocomposite.

spectroscopy. Fig. 7a shows the UV-vis light absorption ability of pristine $\text{g-C}_3\text{N}_4$ and the series of FC nanostructures and it reveals that all the as-prepared nanostructures were capable of absorbing visible light. The UV-vis spectrograph and Tauc plot of pristine Fe_2O_3 is given in Fig. S6. The pristine $\text{g-C}_3\text{N}_4$ exhibits the light absorption edge at

445 nm, it proves its visible light driven photocatalytic performance. Upon loading Fe_2O_3 in the polymeric $\text{g-C}_3\text{N}_4$ structure, the visible light absorption region is significantly increased and the gradual red shift is observed and the obtained band edges of respective materials were tabulated in Table. 4. The series material showed the steady color

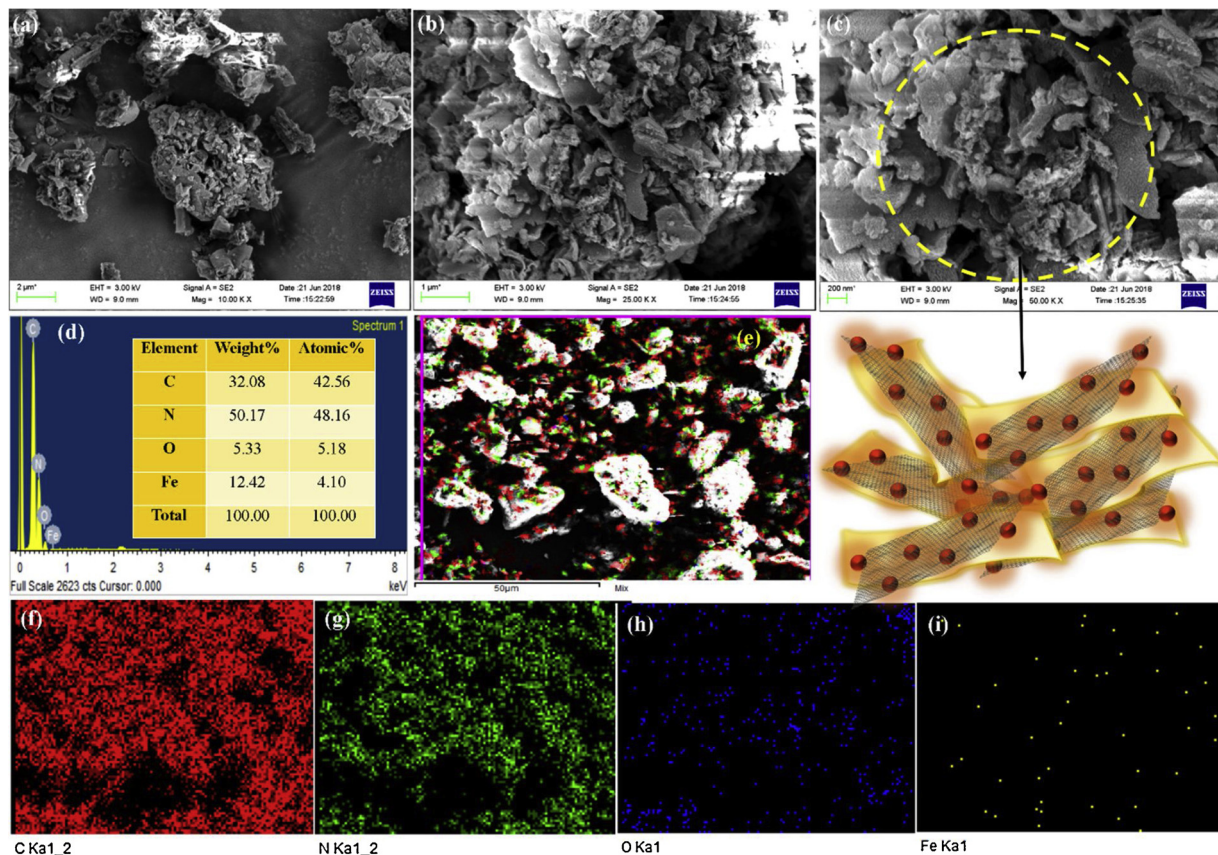


Fig. 6. Morphological analysis: (a–c) FE-SEM micrographs, (d) EDX analysis, (e–i) elemental mapping of 2D/3D/2D-4FC3G ternary nanocomposite.

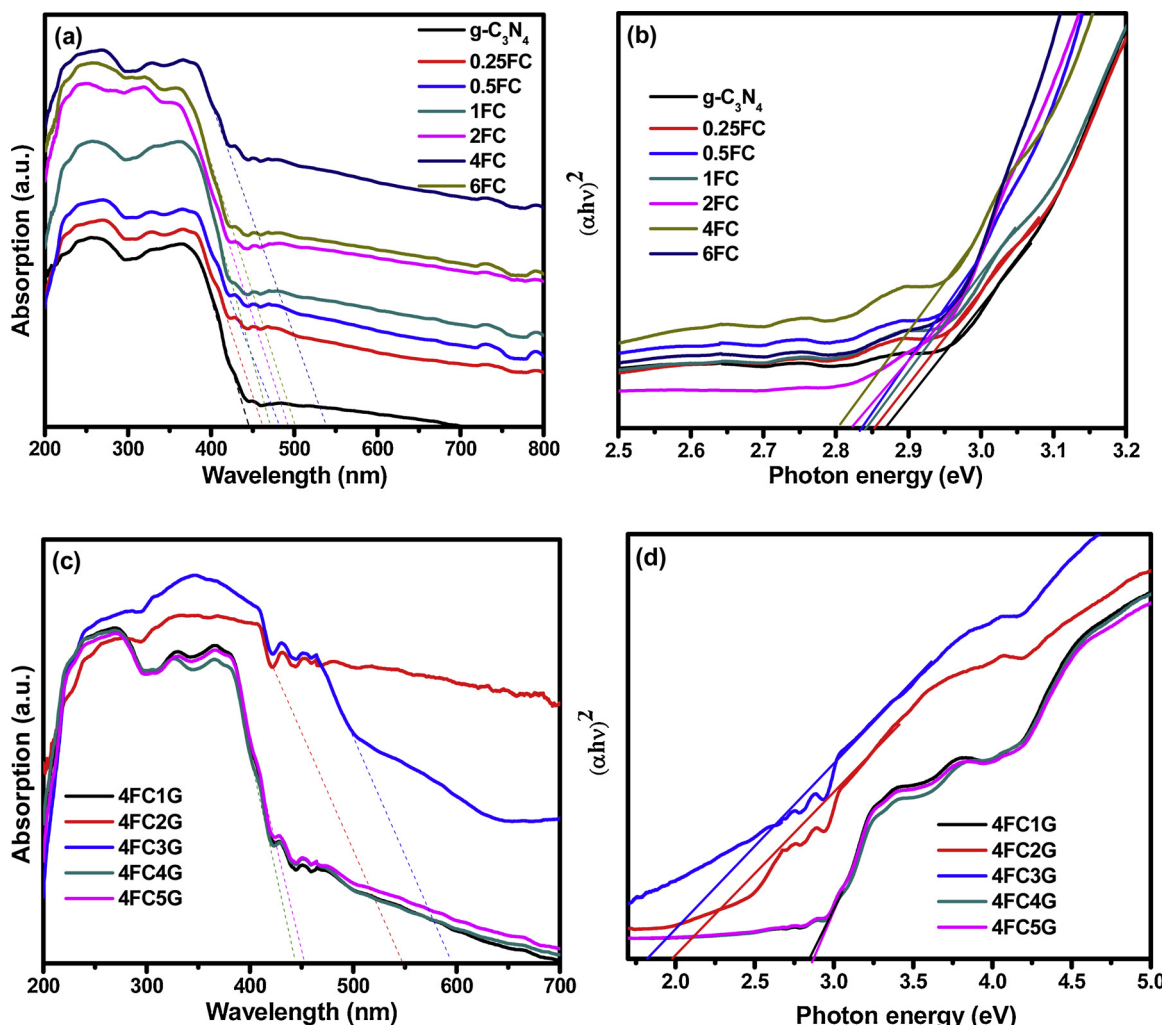


Fig. 7. UV-vis DRS spectrographs: (a) pristine $\text{g-C}_3\text{N}_4$ and 3D/2D- $\text{Fe}_2\text{O}_3/\text{g-C}_3\text{N}_4$ binary nanocomposite (c) 2D/3D/2D-rGO/Fe₂O₃/g-C₃N₄ ternary nanocomposite. Tauc plots: (b) pristine $\text{g-C}_3\text{N}_4$, and 3D/2D- $\text{Fe}_2\text{O}_3/\text{g-C}_3\text{N}_4$ binary nanocomposite (d) 2D/3D/2D-rGO/Fe₂O₃/g-C₃N₄ ternary nanocomposite.

Table 4
Band edge and band gap energies of as-prepared nanostructures.

Sample Code	Band edge (nm)	Band gap energy (eV)
$\text{g-C}_3\text{N}_4$	445	2.86
0.25FC	461	2.85
0.5FC	483	2.83
1FC	471	2.84
2FC	493	2.82
4FC	538	2.80
6FC	501	2.81
4FC1G	459	2.85
4FC2G	564	1.97
4FC3G	597	1.82
4FC4G	445	2.86
4FC5G	455	2.85

change from yellow to reddish yellow and it is due to the good incorporation of Fe_2O_3 nanoparticles with $\text{g-C}_3\text{N}_4$ [8,10]. The maximum visible light absorption ability is observed for 4FC nanostructure with the band edge of about 538 nm. In further, the UV-vis absorption spectra for a series of FCG nanostructures were shown in Fig. 7c. It reveals that while adding rGO with 4FC nanostructure the visible light absorption was highly improved and the change in sample color from reddish yellow to brown is observed [37]. 4FC3G nanostructure showed highest light absorption ability among all other nanostructures. While adding 3% rGO with 4FC, the as-prepared catalyst shows abundant high

intensity in the wavelength range of 400 nm to 800 nm than other as-prepared nanostructures it is due to the improved 2D surface of 4FCG towards visible light. The obtained redshift of the light absorption wavelength for FC and FCG nanostructures enhances the photo-excited electron-hole ($e^- - h^+$) pair generation under visible light irradiation and it will result with the enhanced photocatalytic performance [24]. In case of adding a higher amount of rGO with 4FC, rapid declination of light absorbing ability is observed. The declination in light absorbing ability is may be due to the screening of Fe_2O_3 and $\text{g-C}_3\text{N}_4$ by excess rGO sheets [38]. The light absorption ability of photocatalytic materials was closely related to their optical band gap. In spite to find the band gap energies of as-synthesized pristine $\text{g-C}_3\text{N}_4$, FC and FCG nanostructures Tauc plot was used [22]. The Tauc plot is the graph between $(a\chi h\nu)^2$ and $\chi h\nu$ of nanostructures and it is shown in Fig. 7b,d. The band gap energies were found by extra-plotting a linear line region of the curves in Tauc plot at X-axis. The band gap energies were found by using the same technique for all samples and tabulated in Table 4. Among all as-prepared nanostructures, 2D/3D/2D-4FC3G is found to be the lowest band gap of about 1.82 eV.

3.7. Photocatalytic degradation examination

The photocatalytic carcinogen degradation performance of as-synthesized nanomaterials was evaluated using TC and CP as a model carcinogen under visible light illumination. In order to get a better

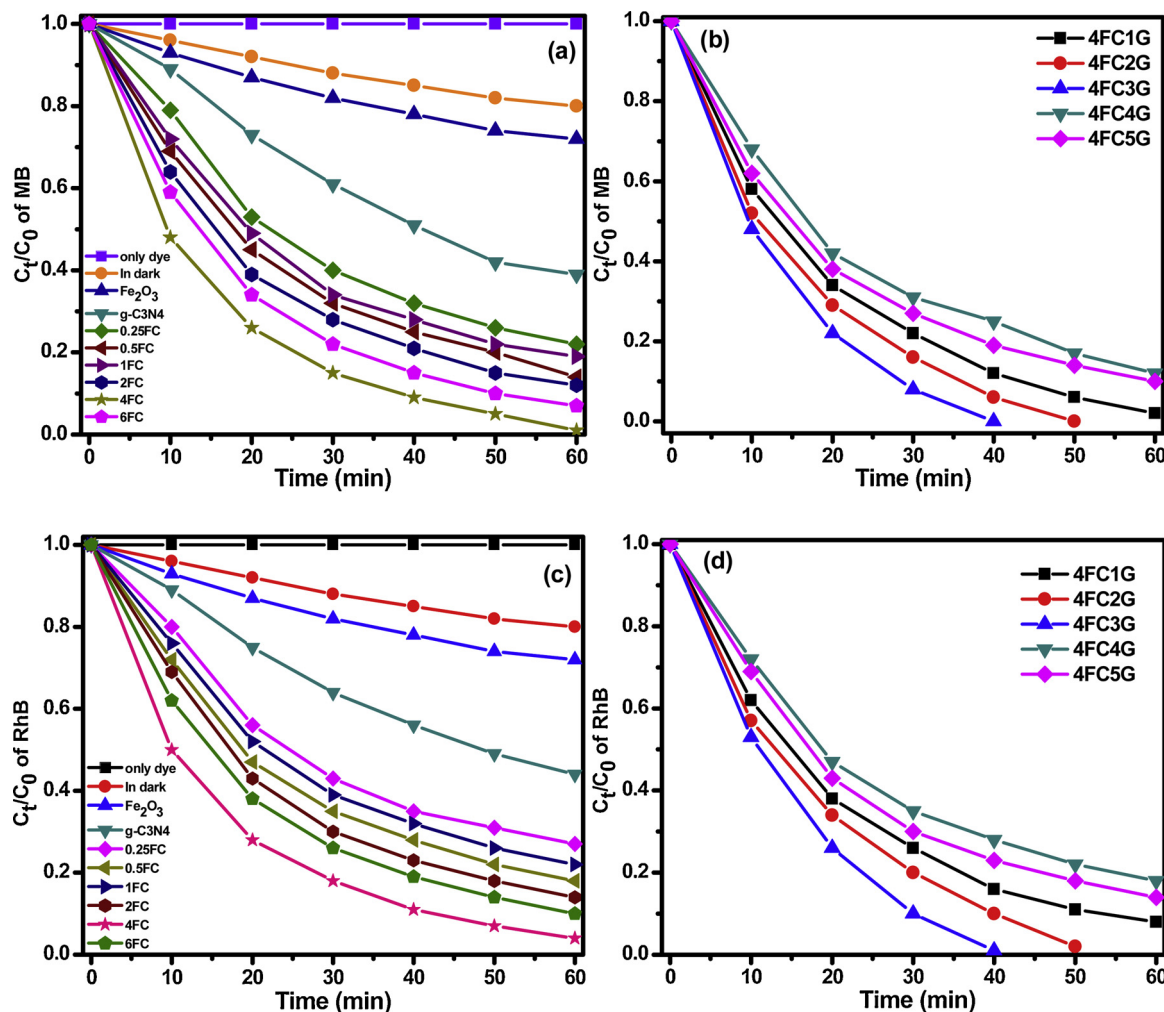


Fig. 8. Photocatalytic degradation rate curves: (a, b) TC and (c, d) CP, in presence of as-prepared nanostructures (photocatalytic reaction conditions: photocatalyst dosage = 100 mg, pharmaceutical molecule concentration = 50 mg/L, pH = 7 and reaction time = 60 min).

photocatalytic efficiency evaluation, the photocatalytic degradation experiments of pristine $\text{g-C}_3\text{N}_4$ and Fe_2O_3 was also carried out. In addition, carcinogen removal experiments were also carried out in the presence of a catalyst without light irradiation to examine carcinogen adsorption ability of catalyst and the self-degradation ability of model carcinogen was also examined by similar experiment in the absence of a catalyst. The photocatalytic degradation efficiency curves of as-synthesized nanostructures were shown in Fig. 8a-d and the UV-Vis spectrum of TC show the declination in spectral intensities with a periodic interval time of photocatalytic degradation (Fig. S7). The obtained results reveal that all $\text{Fe}_2\text{O}_3/\text{g-C}_3\text{N}_4$ nanostructures have enhanced photocatalytic degradation ability than both pristine $\text{g-C}_3\text{N}_4$ and Fe_2O_3 nanostructures. When Fe_2O_3 is doped in $\text{g-C}_3\text{N}_4$ nanosheets the photocatalytic ability is gradually increasing with increasing the dopant concentration of Fe_2O_3 , these results suggest that Fe_2O_3 has a great influence on the photocatalytic degradation of organic carcinogens with $\text{g-C}_3\text{N}_4$ nanosheets. The improvement in photocatalytic efficiency is attributed to the reduction in band gap energy of $\text{Fe}_2\text{O}_3/\text{g-C}_3\text{N}_4$ nanostructures which will increase the visible light absorption ability in parallel [39,40]. The obtained results show the presence of a synergistic effect between Fe_2O_3 and $\text{g-C}_3\text{N}_4$ heterojunction, which can efficiently enhance the photocatalytic activity of $\text{Fe}_2\text{O}_3/\text{g-C}_3\text{N}_4$ nanostructure through facilitated charge carrier separation between heterogeneous interface [41]. Especially, 4% Fe_2O_3 doped $\text{g-C}_3\text{N}_4$ shows higher degradation efficiency of about 98% for TC and 97% for CP which is much higher than other as-synthesized nanostructures (Fig. 8a,c). At the same

time, when Fe_2O_3 concentration increased beyond 4% the photocatalytic degradation ability was rapidly declining, this may depend on two major factors. The excess amount of Fe_2O_3 will affects the separation efficiency of photoexcited charge carriers due to the higher recombination ability of Fe_2O_3 nanoparticles. On the other hand, excess doping of Fe_2O_3 nanoparticles on $\text{g-C}_3\text{N}_4$ nanosheets possibly breaking the laminated structure and it results in the declination of the catalytic surface area [34]. The reduction in catalytic surface area results in the generation of fewer charge carriers, which finally decreasing the photocatalytic performance. As a result, 4% of Fe_2O_3 is found to be optimum doping concentration in enhanced photocatalytic performance. The photocatalytic properties by 4% Fe_2O_3 doped $\text{g-C}_3\text{N}_4$ nanosheets were further improved by introducing rGO sheets. The photocatalytic performance of rGO/ $\text{Fe}_2\text{O}_3/\text{g-C}_3\text{N}_4$ nanocomposite was studied by using the same carcinogen with same photocatalytic reaction parameters and the obtained results were displayed in Fig. 8b,d. The photocatalytic degradation results show that the photocatalytic properties of 4% Fe_2O_3 doped $\text{g-C}_3\text{N}_4$ nanosheets were increased rapidly by adding rGO sheets. This is due to the higher improvement in the presence of higher catalytically active oxygen-containing groups like ketones on the rGO surface. In general, ketonic groups contain a number of electrons which can organize the redox process on the catalytic surface [42]. The CB band edge of the position of rGO sheets is highly recommended as the better trapping of photoexcited electrons on the rGO surface which will drastically reduce the recombination of photoexcited charge carriers of the catalyst [43]. But when the rGO sheets were added above

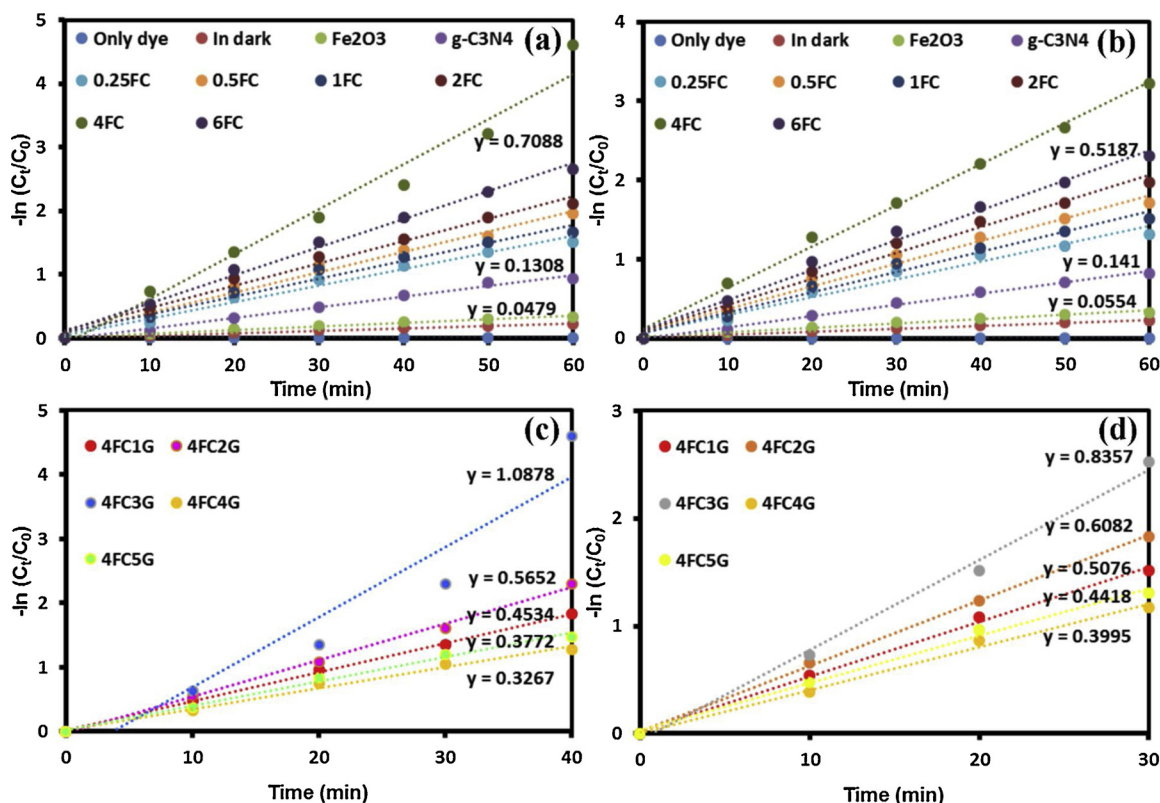


Fig. 9. The pseudo first-order kinetics plots: (a, c) TC and (b, d) CP (photocatalytic reaction conditions: photocatalyst dosage = 100 mg, pharmaceutical molecule concentration = 50 mg/L, pH = 7 and reaction time = 60 min and 30 min).

3% the photocatalytic properties of as-synthesized nanocomposite is slightly affected and it is due to the presence of excess amounts of rGO sheets, screens the Fe₂O₃/g-C₃N₄ photocatalyst which will affect the intensity of incident light on the catalytic surface and hence 3% rGO on 6%Fe₂O₃-C₃N₄ is found to be optimized level for enhanced photocatalytic degradation of organic carcinogens [38].

In order to study the degradation kinetics of TC and CP molecules in the presence of as prepared pristine, 3D/2D FC binary and 2D/3D/2D FCG ternary nanocomposites the pseudo-first-order kinetics relation is used and the equation is $\ln\left(\frac{C_t}{C_0}\right) = k t$ where, k is the apparent pseudo first order photocatalytic degradation rate constant per minute, C_t is the temporal concentration of pharmaceutical molecules and C_0 is the initial concentration of pharmaceutical molecules [44,45]. The photocatalytic degradation kinetics plots of FC and FCG nanocomposite is shown in Fig. 9. The obtained results show that when Fe₂O₃ is doped with g-C₃N₄ nanosheets the photocatalytic degradation efficiency of FC nanostructure was increased more rapidly than pure g-C₃N₄ nanosheets and it is found that the degradation rate constant is maximum at 4% doping of Fe₂O₃ in g-C₃N₄ nanosheets. The apparent photocatalytic degradation rate constant of 4FC is found to be $k = 0.7088 \text{ min}^{-1}$ and $k = 0.5187 \text{ min}^{-1}$ against the degradation of TC and CP respectively. The apparent photocatalytic degradation rate of Pristine Fe₂O₃ is found to be $k = 0.0479 \text{ min}^{-1}$ and $k = 0.0554 \text{ min}^{-1}$ and the results show that the as prepared 4FC nanostructure has 14 times and 10 times higher degradation rate against TC and CP respectively, while comparing with pristine Fe₂O₃. In further, the pseudo first-order kinetics relation is studied for FCG nanosheets and the obtained results suggest that the 3% rGO in 4FC has higher degradation ability than other rGO composites 4FC and the apparent rate constant of 4FC3G is found to be $k = 1.0878$ and $k = 0.8357$ and it is 22 times and 16 times higher than pristine g-C₃N₄ against the degradation of TC and CP respectively. The obtained results clearly show that the 4FC3G has the superior photocatalytic degradation ability against TC and CP molecules degradation

and it is due to the synergistic effect between Fe₂O₃, g-C₃N₄ and rGO.

3.7.1. Effect of initial pH of the photocatalytic reaction solution

The pharmaceutical drug molecules, usually have a different range of pH. Hence, the interaction between the photocatalytic surface and the pharmaceutical drug molecules will be varied based on the pH of the photocatalytic reaction solution [23]. When the number of pharmaceutical drug molecules adsorbed on the surface of 4FC3G photocatalyst the rate of decomposition of drug molecules will be higher. The pH of the photocatalytic reaction solution determines the surface charge the photocatalyst, aggregation size of photocatalyst, hydroxyl radical concentration in the photocatalytic reaction solution and electrostatic attraction of pharmaceutical condemnations on the surface of 4FC3G photocatalyst [46]. In order to study the effect of pH of the reaction solution on the degradation efficiency of 4FC3G photocatalyst, the pH of the photocatalytic reaction solution varies between 2–12 pH. The initial pH of the reaction solution is altered by adding an appropriated amount of NaOH and HCl at 0.2 mol/L concentration. The obtained results in Fig. S8 shows that the 4FC3G photocatalyst has a higher degradation efficiency at higher pH of the photocatalytic reaction solution against TC molecules. The 4FC3G photocatalyst showed the degradation efficiency of about 88% at 7 pH and 92% in 11 respectively. This is due to the presence of the higher amount of hydroxyl ions in the reaction solution which will react with the holes generated in 4FC3G nanocomposite during photoexcitation process results in the formation of a higher amount of hydroxyl radicals (·OH) [47]. In addition, the TC molecules are acidic in nature and hence the absorption of positively charged TC molecules will be higher in the alkaline solution due to the negative charge of 4FC3G nanocomposite surface.

3.7.2. Effect of initial TC concentration and 4FC3G dosage in the photocatalytic reaction solution

The effect of the initial concentration of TC molecules on the

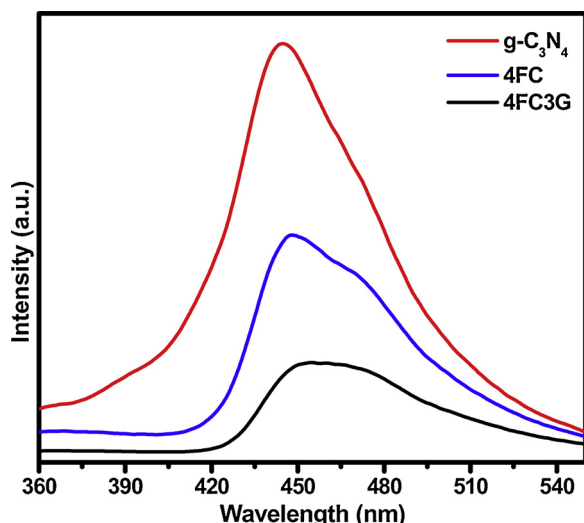


Fig. 10. PL analysis of pristine $\text{g-C}_3\text{N}_4$, pristine Fe_2O_3 , 4FC binary and 4FC ternary nanocomposite.

degradation efficiency of the 4FC3G photocatalyst is studied to find the dependence of initial TC concentration on the photocatalytic degradation ability of 4FC3G nanocomposite. **Fig. S9a** shows the photocatalytic degradation efficiency of 4FC3G nanocomposite at different initial TC concentration from 10 mg/l to 50 mg/L. The obtained results show that the 4FC3G nanocomposite has a higher degradation ability at lower TC concentration. When the concentration of TC in the photocatalytic reaction is increased the photocatalytic degradation efficiency of 4FC3G nanocomposite is gradually decreased from 98% at 10 mg/l of TC to 60% at 50 mg/l of TC. The degradation of TC molecules is highly dependent on the formation of ·OH on the surface of the 4FC3G composite and the chance of reaction between TC molecules and generated ·OH. In addition, at higher concentration of TC molecules in the reaction solution, the intensity of the photons entering the reaction solution decreases and its results with the less absorption of photons by the 4FC3G composite [22,34]. The lower absorption of photons by 4FC3G composite directly affect the degradation rate of TC molecules. The adsorption of O_2 and ·OH on the 4FC3G surface will also affect at a higher initial concentration of TC molecules due to the higher amount of TC molecule adsorption on the surface of the 4FC3G catalyst. The effect of initial 4FC3G dosage on the degradation of TC is also studied with a different initial 4FC3G dosage of 0.5 g/100 ml to 1.5 g/100 ml and the obtained results were shown in **Fig. S9b**. The 4FC3G photocatalyst showed 52% and 99% of degradation efficiency at 0.5 g/100 ml and 1.5 g/100 ml, respectively. This is due to the higher availability of the total active surface area of 2D/3D/2D 4FC3G photocatalyst at its highest dosage [48]. In addition, the density of 4FC3G photocatalyst in the visible light illuminating will increase the light harvesting probability and its results with the higher production of active species for TC molecule degradation.

3.8. OH radicals production analysis

The ·OH radical production efficiency of as-prepared 4FC3G nanostructure was assessed by using terephthalic acid (TA) as a non-fluorescent probe molecule. The PL technique is utilized to detect the ·OH radical generation during the photocatalytic process of 4FC3G nanocomposite under white LED irradiation. The reaction process of ·OH radical estimation analysis is explained in the above experimental section. The ·OH radicals generated during the 4FC3G involved photocatalytic process will react with TA molecules present in the reaction solution and it gets converted into hydroxyterephthalic acid (HTA) molecules. In nature, TA is a non-fluorescent molecule, but in the case

of hydroxyterephthalic acid (HTA), it shows florescent property with a maximum peak at $\lambda = \sim 425$ nm [23,25]. Initially, the PL analysis results show the blank spectral curve without any emission at time 0 min, it shows the nonexistence of HTA molecules in the reaction solution. The formation of HTA molecules is clearly identified by respective PL spectra of HTA molecules by evaluation of time from 0 min to 30 min **Fig. S10**. The peak intensity at $\lambda = \sim 425$ nm is consecutively increased with the increment of time it clearly reflects the enhanced production of ·OH radicals during the photocatalytic process.

3.9. Photocatalytic mechanism

The highly enhanced photocatalytic ability of as prepared 4FC3G nanocomposites encourages us to further study its photocatalytic degradation reaction mechanism. The construction of 2D/3D/2D-rGO/ $\text{Fe}_2\text{O}_3/\text{g-C}_3\text{N}_4$ nanocomposite has the remarkable photocatalytic degradation ability towards the pharmaceutical pollutants. The highly enhanced activity of 2D/3D/2D nanocomposite will create a novel idea towards the designing and synthesis of 2D and 3D materials composed ternary nanostructures with an efficient catalytic ability. In order to study the effect of 2D/3D/2D geometric structure on the catalytic ability of 4FC3G, it is very important to understand the origin of highly improved photocatalytic degradation performance. It is well known that optical absorption ability, photoinduced charge migration and separation efficiency of the catalytic materials are the most predominant scientific factors for better photocatalytic ability [24,26,33]. Hence, it is necessary to study and explore the intrinsic relation between these scientific issues and the catalytic pharmaceutical degraded performance of 2D/3D/2D-rGO/ $\text{Fe}_2\text{O}_3/\text{g-C}_3\text{N}_4$ nanocomposite. At first, the photon absorption ability of the nanocomposite is studied and discussed in the above sections, and the obtained results showed that 4FC3G has a steep photon absorption edge at 597 nm and the corresponding band gap energy is estimated to be 1.82 eV, it shows the efficient absorption of solar light.

In addition, the photoinduced charge carrier separation efficiency of the as-synthesized photocatalyst was studied through photoluminescence (PL) analysis. The PL spectra of as-synthesized photocatalyst $\text{g-C}_3\text{N}_4$, 4FC and 4FC3G are shown in **Fig. 10** and PL spectra of pristine Fe_2O_3 nanostructure is shown in **Fig. S11**. The obtained results show the high intense broad photoluminescence peak at 441 nm corresponds to pristine $\text{g-C}_3\text{N}_4$ nanosheets [5]. Such high intensity suggests that pristine $\text{g-C}_3\text{N}_4$ nanosheets have high photoinduced charge carriers recombination rate and it is due to the intrinsic geometrical structure of $\text{g-C}_3\text{N}_4$ [49]. When $\text{g-C}_3\text{N}_4$ is composed with Fe_2O_3 , a slight red shift can be observed in the PL curve of 4FC nanostructure it indicates the shrinking of the band gap and the PL intensity is quenched due to the suppression of photoinduced charge carrier recombination to a particular limit [25]. With more impression, when another 2D structure/rGO is introduced with 4FC nanocomposite the fluorescence of 2D/3D/2D-4FC3G nanocomposite was quenched dramatically and it indicated the advantages of 2D/3D/2D heterojunction on the suppression of photoinduced charge carrier recombination and the migration of charge carriers from the surface of nanostructures [50]. Such higher quenching of photoinduced charge carrier recombination clearly representing that the formation of 2D/3D/2D heterojunction with faster-photoinduced charge transfer nanonetworks highly accelerates the photoinduced charge carrier separation and migration.

In General, hydroxyl radicals ($\cdot\text{OH}$), holes (h^+) and superoxide radicals (O_2^-) are known to be the important reactive species involved during the degradation of organic molecules. In order to determine the predominant reactive species involved in the photocatalytic degradation reaction process, radical trapping experiment is conducted and shown in **Fig. S12**. In this trapping experiment, BQ, TEOA and IPA were used as O_2^- , h^+ and ·OH radical suppressor, respectively [50]. The photocatalytic degradation of TC is decreased rapidly while adding BQ and TEOA. But, the addition of IPA does not affect the degradation

efficiency as like as BQ and TEOA, however, the activity was decreased slightly. While comparing with TEOA, addition BQ in degradation reaction solution has highly affected the photocatalytic degradation of TC molecules and hence it shows that during degradation TC molecules in presence of 4FC3G nanocomposite O_2^- plays a major role than h^+ and $\cdot\text{OH}$ radicals. But both h^+ and O_2^- are the predominant reactive species in this photocatalytic degradation reaction and the obtained results well coincided with the previous research reports. Furthermore, the photocatalytic degradation of TC molecules in presence of 4FC3G is affected more significantly with the addition of BQ and TEOA and this may be due to the highly effective separation and migration of photoinduced charge carriers [8,35].

The involvement of $\cdot\text{OH}$ radicals in the reaction process was further examined by a 5-dimethyl-1-pyrroline-N-oxide (DMPO) trapping EPR method [51]. The experiment was carried out in an aqueous suspension containing 4FC3G: 100 mg /100 ml, TC: 30 mg/l and reaction time: 25 min. As displayed in Fig. S13 EPR signals of DMPO $\cdot\text{OH}$ adduct in the presence of the samples after irradiation for 120 S. The strongest DMPO- $\cdot\text{OH}$ signal was observed in the presence of the 4FC3G nanocomposite. These results clearly demonstrate the enhanced activity of the 4FC3G nanocomposite to produce $\cdot\text{OH}$ radicals than the individual component. Therefore, the outputs of strong oxidizing radicals can be directly recorded by the EPR curve, which determines the photocatalytic performance of the resulting photocatalyst.

The possible photocatalytic mechanism scheme of 2D/3D/2D-4FC3G nanocomposite is shown in Fig. 11. As we discussed above, the higher photon absorption ability and the lower recombination rate of photoexcited charge carriers of as-prepared nanocomposite makes it a better candidate for enhanced photocatalytic performance [4]. In addition, appropriate band edges of the photocatalytic materials are much important to produce a large number of reactive species which are responsible for the degradation of organic molecules. During the photocatalytic process, the electrons excited from valance band (VB) to the conduction band (CB) of photocatalytic materials will utilize by dissolved oxygen molecules in the reaction solution to produce O_2^- radicals. At the same instant, the excited electrons will leave h^+ on the valance band of photocatalytic materials and thus created h^+ in VB gets foraged to form $\cdot\text{OH}$ radicals by hydroxyl groups. In addition, the h^+ generated on the VB of photocatalytic materials has an ability to oxidize the pharmaceutical molecules directly [52]. The radicals like O_2^- , $\cdot\text{OH}$ and h^+ generated during the complete photoexcited e^- - h^+ pair transfer cycle will be utilized for pharmaceutical molecule degradation. The recombination of e^- - h^+ pair plays a major role in the efficiency of

photocatalytic materials where the decrement in e^- - h^+ pair recombination rate will rapidly increase the production of reactive species [5]. The process of e^- - h^+ pair recombination depends upon the band edge positions of photocatalytic materials. The valence band (VB) and conduction band (CB) edges of as-prepared 2D/3D/2D-4FC3G nanocomposite was determined by using the equations as follows $E_{\text{CB}} = \chi - E^{\circ} - 0.5 E_{\text{bg}}$ and $E_{\text{VB}} = E_{\text{CB}} + E_{\text{bg}}$, where E_{CB} and E_{VB} are the conduction band and valance band energy of the photocatalytic material, E° is the energy of free electrons (4.5 eV) on the hydrogen scale, χ is the absolute electronegativity of photocatalytic material and E_{bg} is the energy band gap of the photocatalyst [22]. The absolute electronegativity (χ) of $\text{g-C}_3\text{N}_4$ and Fe_2O_3 was found to be 4.73 eV and 5.88 eV, respectively. Using the above equation the VB and CB edge potentials of $\text{g-C}_3\text{N}_4$ are found to be 1.66 eV Vs Normal Hydrogen Electrode (NHE) and -1.20 eV Vs NHE and VB and CB edge potentials of Fe_2O_3 are found to be 2.53 eV Vs NHE and 0.23 eV Vs NHE, respectively and the Fermi level of rGO nanosheets was found to be (-0.08 eV vs NHE). Based on the band edge positions of $\text{g-C}_3\text{N}_4$ and Fe_2O_3 nanostructures, the formation of Z-scheme heterojunction interface between the nanostructures was confirmed and provides the requirement for the generation of 2D/3D/2D heterojunction with surplus nanochannels for photoexcited charge transfer [5]. When 2D/3D/2D-4FC3G nanocomposite is illuminated by visible light irradiation, the VB electrons from both $\text{g-C}_3\text{N}_4$ and Fe_2O_3 nanostructures will be excited to form enormous amount of e^- - h^+ pairs Fig. 12a. The VB electrons of $\text{g-C}_3\text{N}_4$ nanosheets will be transferred its CB of $\text{g-C}_3\text{N}_4$ and the CB electrons of Fe_2O_3 nanostructure will transfer to the VB of C_3N_4 nanosheets during recombination due to their appropriate band edge potentials. The excited electrons at CB of $\text{g-C}_3\text{N}_4$ nanosheets will be transferred to the Fermi level of rGO nanosheets for a protracted lifetime due to the Fermi level position (-0.08 eV vs NHE) of rGO nanosheets [42]. The transportation of VB electrons ($\text{g-C}_3\text{N}_4$) and CB electrons (Fe_2O_3) nanostructures occurs due to a large number of nanochannels in between 2D/3D/2D-rGO/ Fe_2O_3 / $\text{g-C}_3\text{N}_4$ heterojunctions Fig. 12b. The transportation of photoexcited charge carriers through 2D/3D/2D heterojunction will successively decline the recombination rate of e^- - h^+ pair by delocalizing the electrons excited from the $\text{g-C}_3\text{N}_4$ and Fe_2O_3 nanostructures [8]. The rapid transfer of charge carriers through nanochannels occurred by 2D/3D/2D heterojunction will effectively suppress the charge migration distance and recombination time, with significant enhancement of charge separation and transportation efficiency, will lead to the enhanced production of O_2^- , $\cdot\text{OH}$ and h^+ reactive species for effective degradation of organic molecules [53,54]. The possible transportation

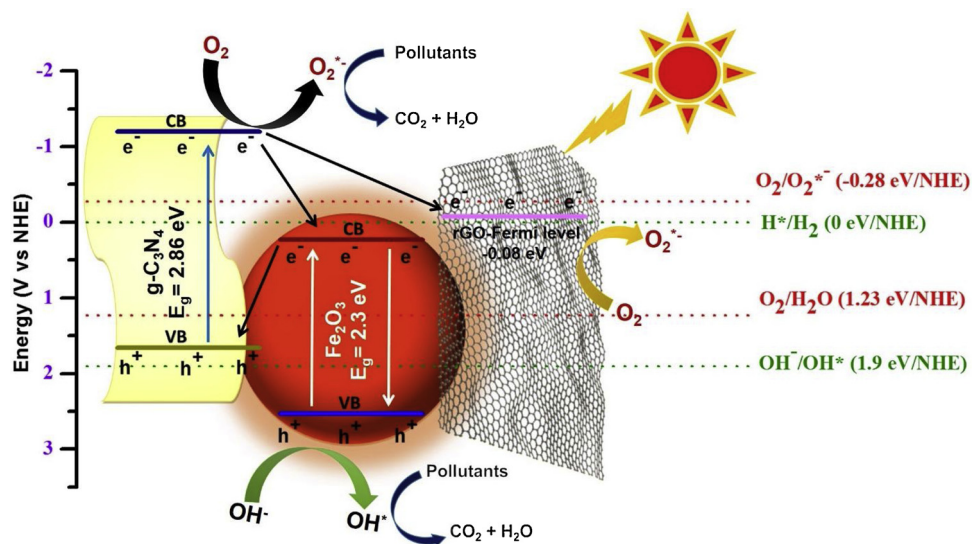


Fig. 11. Proposed photocatalytic mechanism of as-prepared 2D/3D/2D-4FC3G ternary nanocomposite.

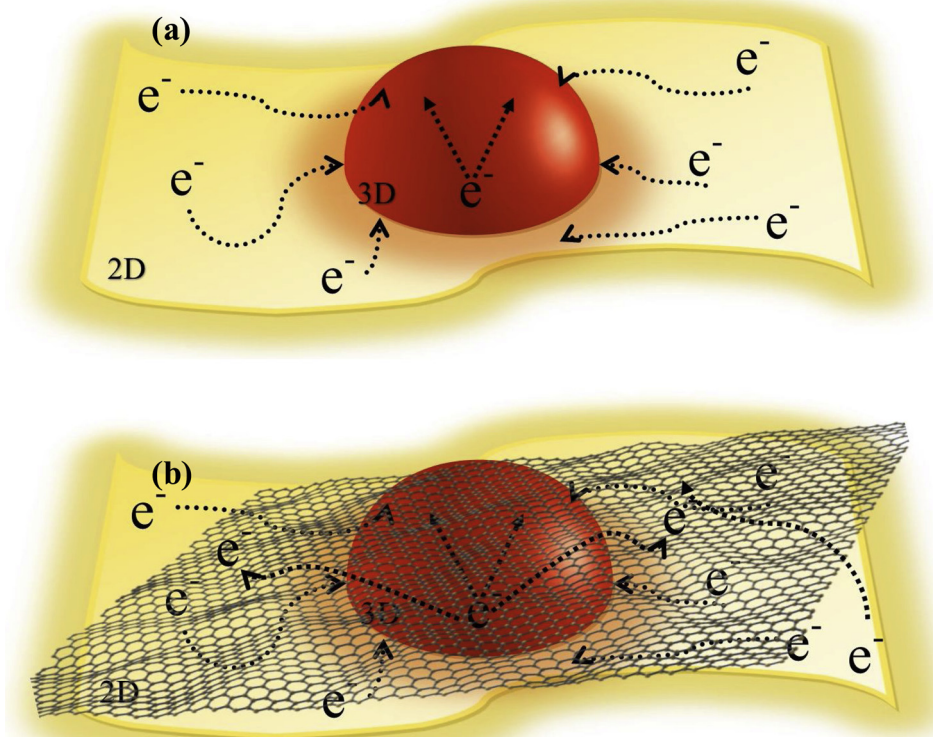
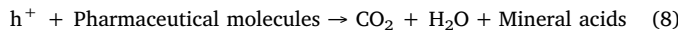
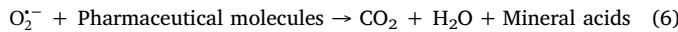
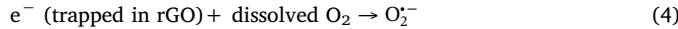
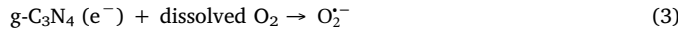
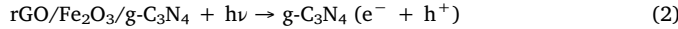
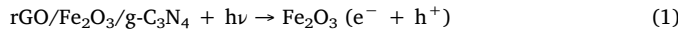


Fig. 12. Schematic illustration: (a) 3D/2D heterojunction contact reference and (b) 2D/3D/2D heterojunction contact reference.

and delocalization pathway of photoexcited charge carriers in 4FC3G photocatalyst will follow as given in the Eqs (1)–(8):



The above-given transfer and separation pathway of charge carriers in 2D/3D/2D heterojunction of 4FC3G ternary nanocomposite leads to superior production of O_2^- , h^+ and $\cdot\text{OH}$ reactive species for effective pharmaceutical molecules degradation.

3.10. Photocatalytic degradation pathway of CP

The degradation of the pharmaceutical complex is multifaceted with the formation of several intermediate molecules and it is necessary to understand the possible degradation pathways of CP, in order to identify the prime degradation intermediates produced during the photocatalytic degradation reaction. In order to detect the prime intermediates formed during the photocatalytic degradation reaction and to understand the degradation of CP molecules, LC-TOF/MS analysis technique was employed. The possible photocatalytic degradation pathways of CP molecules are shown in Fig. 13. By using LC-TOF/MS analysis six different degradation molecule intermediates were found with $m/z = 245, 263, 285, 288, 330, 340, 291, 306, 334$ and 362 (Fig.

S14). The obtained LC-TOF/MS analysis suggests that initially, the piperazine ring gets fragmented before quinolone moiety with the formation of two other intermediate molecules with m/z of about 340 and 288 [1]. The formation of these intermediate molecules represents the removal of ketone and carboxylic groups at the quinolone moieties. Based on the above results, it is suggested that the degradation of CP follows three pathways to degrade completely. The first pathway as shown in Fig. 13 is the prime degradation pathway of CP molecules in this photocatalytic degradation reaction. Initially, the piperazine ring in the CP ($m/z = 332$) molecule is cracking down to form first intermediate molecule CP1 ($m/z = 362$) and further degrades to CP2 ($m/z = 306$) with the removal of two carboxylic groups (C=O). Simultaneously, the intermediate molecule CP2 ($m/z = 306$) reacts with the $\cdot\text{OH}$ radicals to produce CP3 ($m/z = 291$) by the hydroxylation and further removal of CH-NH₂ was occurred to form CP4 ($m/z = 263$). The degradation intermediate CP4 ($m/z = 263$) is formed by releasing C=O from CP3, followed by the formation of CP5 ($m/z = 245$) intermediate by the defluorination process. In the second pathway of CP degradation, the couple of intermediates CP8 ($m/z = 340$) and CP7 ($m/z = 288$) is produced [55]. The photoinduced h^+ radical will react with the quinolone moiety of CP molecule and its results with the decarboxylation of CP molecules to produce CP7 ($m/z = 288$) followed by the splitting of adjacent C=C group to produce a carboxylic acid group forming CP8 ($m/z = 340$) and CP6 ($m/z = 334$) [56]. The hydroxyl-substituted fluorine intermediate CP9 ($m/z = 334$) is formed by the reaction of CP molecule with the OH radical and gets further degraded into CP10 ($m/z = 330$), with the continuous photocatalytic degradation reaction some of the reaction intermediates breakdowns into producing several other smaller substances followed by the mineralization to form CO₂ and H₂O.

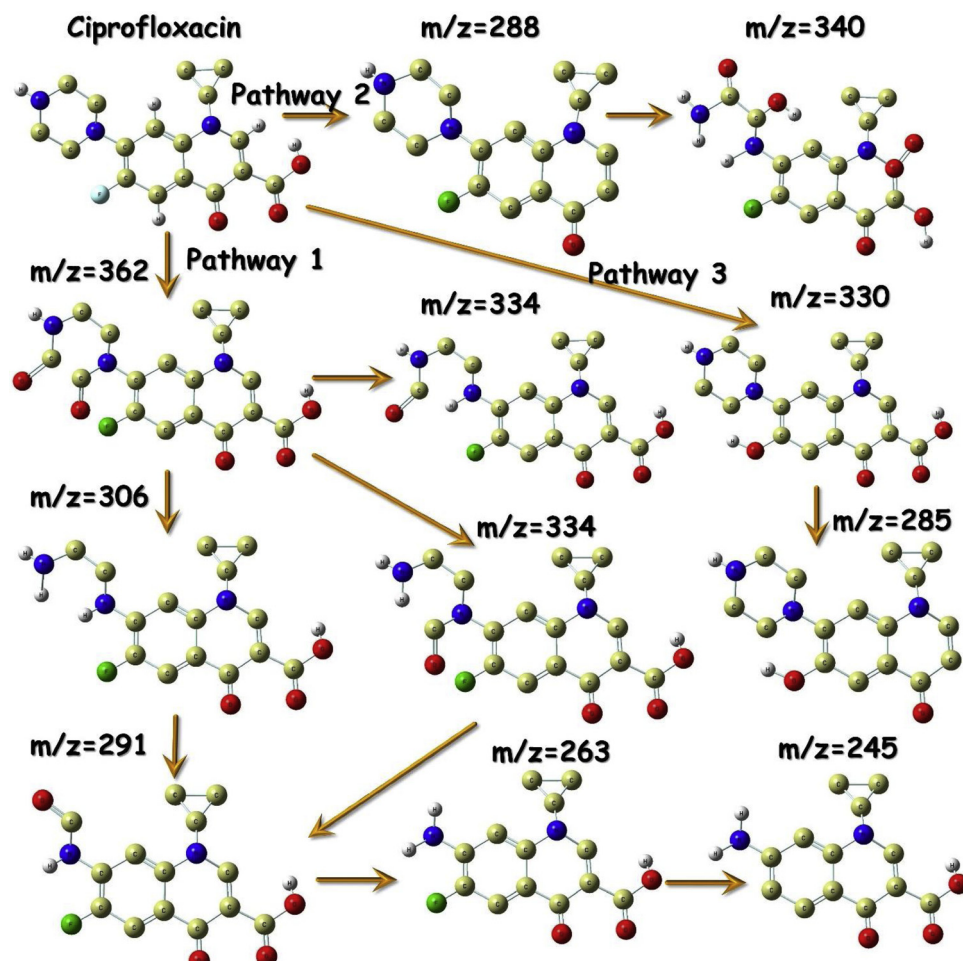


Fig. 13. The proposed photocatalytic degradation pathway of CP molecules in 2D/3D/2D rGO/Fe₂O₃/g-C₃N₄.

3.11. Stability analysis of 2D/3D/2D-4FC3G ternary nanocomposite

The photocatalytic stability and recyclability is the prime parameter for its real-life applications. It shows the ability of photocatalyst for long time successive photocatalytic reactions. The high stability of photocatalyst will significantly lead to cost reduction during the contamination removal process at large scale applications. The photocatalytic stability and recyclability of the 4FC3G nanocomposite were analyzed by five successive cyclic photocatalytic degradation experiments and shown in Fig. 14a. The stability analysis is carried out for 200 min with 40 min for each cycle under the typical photoreaction

procedure as explained above. The obtained cyclic results show a very small reduction in the photocatalytic ability of 4FC3G after five successive degradation cycles of TC molecules. The efficiency of the 4FC3G nanosheets was decreased only 4% after five cycles of TC molecule degradation and it shows that the 4FC3G nanocomposite is highly stable in nature. The XRD spectrograph of reused 4FC3G nanocomposite is shown in Fig. 14b, it shows that 4FC3G nanocomposite has a highly stable structure with a very minute reduction in its catalytic ability even after five cycles of photocatalytic degradation. These obtained results clearly indicated that the g-C₃N₄, Fe₂O₃ and rGO is well composed with each other with the strong binding of Fe₂O₃ on the

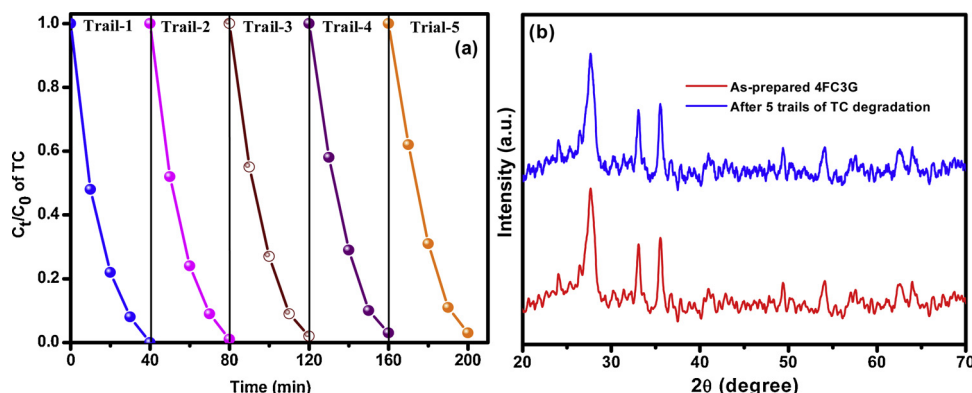


Fig. 14. Photodegradation stability analysis of the as-prepared 2D/3D/2D-4FC3G nanocomposite upon degrading of TC molecules: (a) cyclic degradation rate curves (b) XRD spectrograph of 4FC3G photocatalyst after the 5th trail of TC degradation.

surface of electron rich $\text{g-C}_3\text{N}_4$ and rGO nanosheets. Hence, 4FC3G nanocomposites can be utilized as a potentially reusable photocatalytic material with an enhanced photocatalytic performance for real-time pharmaceutical molecule degradation.

4. Conclusion

In summary, a series of visible-light driven 3D/2D $\text{Fe}_2\text{O}_3/\text{g-C}_3\text{N}_4$ and 2D/3D/2D rGO/ $\text{Fe}_2\text{O}_3/\text{g-C}_3\text{N}_4$ nanocomposite has been well designed and successfully prepared through two-step hydrothermal technique using RSM methodology. The structural, morphological, optical absorption and elemental chemical state analysis of the as-prepared 2D/3D/2D rGO/ $\text{Fe}_2\text{O}_3/\text{g-C}_3\text{N}_4$ nanocomposite confirm the formation of 2D/3D/2D heterojunction with a strong interaction between 3D/2D $\text{Fe}_2\text{O}_3/\text{g-C}_3\text{N}_4$ and 2D rGO nanosheets. The UV-vis DRS and PL study reveal that the formation of visible-light driven 2D/3D/2D heterojunction has created numerous nanochannels for rapid transportation of photoexcited charge carriers and it drastically inhibited the recombination rate of photoexcited charge carriers with significant enhancement of charge separation and transportation efficiency. The photocatalytic properties of as-prepared 3D/2D and 2D/3D/2D heterojunction were studied well against the degradation of emerging pharmaceutical contaminations like tetracycline and ciprofloxacin molecules. The composition of 3% rGO in 4% $\text{Fe}_2\text{O}_3/\text{g-C}_3\text{N}_4$ nanostucture exhibited the highest photocatalytic ability with strong stability and recyclability. The photocatalytic mechanism of 2D/3D/2D heterojunction was proposed based on UV-vis DRS, PL, EPR, reactive species trapping experiment and $\cdot\text{OH}$ radical production analysis. This research work provides a new path for the design and production of 2D/3D/2D heterojunction photocatalyst with supreme charge carrier separation and migration ability.

Appendix A. Supplementary data

Supplementary material related to this article can be found, in the online version, at doi:<https://doi.org/10.1016/j.apcatb.2019.117758>.

References

- [1] Y.C. Nie, F. Yu, L.C. Wang, Q.J. Xing, X. Liu, Y. Pei, J.P. Zou, W.L. Dai, Y. Li, S.L. Suib, Photocatalytic degradation of organic pollutants coupled with simultaneous photocatalytic H₂ evolution over graphene quantum dots/Mn-N-TiO₂/g-C₃N₄ composite catalysts: performance and mechanism, *Appl. Catal. B Environ.* 227 (2018) 312–321, <https://doi.org/10.1016/j.apcatb.2018.01.033>.
- [2] C. Wang, Y. Wu, J. Lu, J. Zhao, J. Cui, X. Wu, Y. Yan, P. Huo, Bioinspired synthesis of photocatalytic nanocomposite membranes based on synergy of Au-TiO₂ and polydopamine for degradation of tetracycline under visible light, *ACS Appl. Mater. Interfaces* 9 (2017) 23687–23697, <https://doi.org/10.1021/acsami.7b04902>.
- [3] Y. Gong, X. Quan, H. Yu, S. Chen, H. Zhao, Enhanced photocatalytic performance of a two-dimensional BiO_{1-x}_x/g-C₃N₄ heterostructured composite with a Z-scheme configuration, *Appl. Catal. B Environ.* 237 (2018) 947–956, <https://doi.org/10.1016/j.apcatb.2018.06.060>.
- [4] Z. Li, Z. Zhou, J. Ma, Y. Li, W. Peng, G. Zhang, F. Zhang, X. Fan, Hierarchical photocatalyst of In₂S₃ on exfoliated MoS₂ nanosheets for enhanced visible-light-driven Aza-Henry reaction, *Appl. Catal. B Environ.* 237 (2018) 288–294, <https://doi.org/10.1016/j.apcatb.2018.05.087>.
- [5] B. Lin, H. Li, H. An, W. Hao, J.J. Wei, Y. Dai, C. Ma, G. Yang, Preparation of 2D/2D g-C₃N₄ nanosheet@ZnIn₂S₄ nanoleaf heterojunctions with well-designed high-speed charge transfer nanochannels towards high-efficiency photocatalytic hydrogen evolution, *Appl. Catal. B Environ.* 220 (2018) 542–552, <https://doi.org/10.1016/j.apcatb.2017.08.071>.
- [6] C. Xue, X. Yan, H. An, H. Li, J. Wei, G. Yang, Bonding CdS-Sn₂S₃ eutectic clusters on graphene nanosheets with unusually photoreaction-driven structural reconfiguration effect for excellent H₂ evolution and Cr (VI) reduction, *Appl. Catal. B* 222 (2018) 157–166, <https://doi.org/10.1016/j.apcatb.2017.10.008>.
- [7] X. Liu, A. Jin, Y. Jia, J. Jiang, N. Hu, X. Chen, Facile synthesis and enhanced visible-light photocatalytic activity of graphitic carbon nitride decorated with ultrafine Fe₂O₃ nanoparticles, *RSC Adv.* 5 (2015) 92033–92041, <https://doi.org/10.1039/c5ra18466e>.
- [8] S. Tonda, S. Kumar, S. Kandula, V. Shanker, Fe-doped and -mediated graphitic carbon nitride nanosheets for enhanced photocatalytic performance under natural sunlight, *J. Mater. Chem. A Mater. Energy Sustain.* 2 (2014) 6772–6780, <https://doi.org/10.1039/c3ta15358d>.
- [9] Y. Lei, C.S. Chen, Y.J. Tu, Y.H. Huang, H. Zhang, Heterogeneous degradation of organic pollutants by persulfate activated by CuO-Fe₂O₃: mechanism, stability, and effects of pH and bicarbonate ions, *Environ. Sci. Technol.* 49 (2015) 6838–6845, <https://doi.org/10.1021/acs.est.5b00623>.
- [10] J. Wang, C. Li, J. Cong, Z. Liu, H. Zhang, M. Liang, J. Gao, S. Wang, J. Yao, Facile synthesis of nanorod-type graphitic carbon nitride/Fe₂O₃ composite with enhanced photocatalytic performance, *J. Solid State Chem.* 238 (2016) 246–251, <https://doi.org/10.1016/j.jssc.2016.03.042>.
- [11] Y. Liu, N. Sun, J. Hu, S. Li, G. Qin, Photocatalytic degradation properties of α -Fe₂O₃ nanoparticles for dibutyl phthalate in aqueous solution system, *R. Soc. Open Sci.* 5 (2018), <https://doi.org/10.1098/rsos.172196>.
- [12] R. Li, Y. Jia, N. Bu, J. Wu, Q. Zhen, Photocatalytic degradation of methyl blue using Fe₂O₃/TiO₂ composite ceramics, *J. Alloys. Compd.* 643 (2015) 88–93, <https://doi.org/10.1016/j.jallcom.2015.03.266>.
- [13] X. Chao, H. An, G. Yang, Facile construction of MoS₂/CdS eutectic clusters anchored on rGO edge with enhanced hydrogen generation performance, *Catal. Today* 317 (2018) 99–107, <https://doi.org/10.1016/j.cattod.2018.01.023>.
- [14] L. Liu, J. Wang, C. Wang, G. Wang, Facile synthesis of graphitic carbon nitride/nanostructured α -Fe₂O₃ composites and their excellent electrochemical performance for supercapacitor and enzyme-free glucose detection applications, *Appl. Surf. Sci.* 390 (2016) 303–310, <https://doi.org/10.1016/j.apsusc.2016.08.093>.
- [15] J. Gao, Y. Wang, S. Zhou, W. Lin, Y. Kong, A facile one-step synthesis of Fe-doped g-C₃N₄ nanosheets and their improved visible-light photocatalytic performance, *ChemCatChem.* 9 (2017) 1708–1715, <https://doi.org/10.1002/ctc.201700492>.
- [16] Y. Peng, W. Pan, N. Wang, J.E. Lu, S. Chen, Ruthenium ion-complexed graphitic carbon nitride nanosheets supported on reduced graphene oxide as high-performance catalysts for electrochemical hydrogen evolution, *ChemSusChem.* 11 (2018) 4, <https://doi.org/10.1002/cssc.201702375>.
- [17] P. Tiong, H.O. Lintang, S. Endud, L. Yulianti, Improved interfacial charge transfer and visible light activity of reduced graphene oxide-graphitic carbon nitride photocatalysts, *RSC Adv.* 5 (2015) 94029–94039, <https://doi.org/10.1039/c5ra17967j>.
- [18] C. Xue, H. Li, H. An, B. Yang, J. Wei, G. Yang, NiS_x quantum dots accelerate electron transfer in Cd_{0.8}Zn_{0.2}S photocatalytic system via an rGO nanosheet “Bridge” toward visible-light-driven hydrogen evolution, *ACS Catal.* 8 (2018) 1532–1545, <https://doi.org/10.1021/acscatal.7b04228>.
- [19] J. Xue, S. Ma, Y. Zhou, Z. Zhang, M. He, Facile photochemical synthesis of Au/Pt/g-C₃N₄ with plasmon-enhanced photocatalytic activity for antibiotic degradation, *ACS Appl. Mater. Interfaces* 7 (2015) 9630–9637, <https://doi.org/10.1021/acsami.5b01212>.
- [20] Y. Che, B. Lu, Q. Qi, H. Chang, J. Zhai, K. Wang, Z. Liu, Bio-inspired Z-scheme g-C₃N₄/Ag₃CrO₄ for efficient visible-light photocatalytic hydrogen generation, *Sci. Rep.* 8 (2018) 1–12, <https://doi.org/10.1038/s41598-018-34287-w>.
- [21] A. Asfaram, M. Ghaedi, S. Agarwal, I. Tyagi, V.K. Gupta, Removal of basic dye Auramine-O by Zn_xCu nanoparticle loaded on activated carbon: optimization of parameters using response surface methodology with central composite design, *RSC Adv.* 5 (2015) 18438–18450, <https://doi.org/10.1039/c4ra15637d>.
- [22] S. Shanavas, A. Priyadharsan, V. Vasanthakumar, A. Arunkumar, P.M. Anbarasan, S. Bharathkumar, Mechanistic investigation of visible light driven novel La₂CuO₄/CeO₂/rGO ternary hybrid nanocomposites for enhanced photocatalytic performance and antibacterial activity, *J. Photochem. Photobiol. A: Chem.* 340 (2017) 96–108, <https://doi.org/10.1016/j.jphotochem.2017.03.002>.
- [23] S. Shanavas, A. Priyadharsan, K. Dharmaboopathi, I. Ragavan, C. Vidya, P.M. Anbarasan, Ultrasonically and photonically simulatable Bi-Ceria nanocubes for enhanced catalytic degradation of aqueous dyes: a detailed study on optimization, mechanism and stability, *ChemistrySelect.* 3 (2018) 12841–12853, <https://doi.org/10.1002/slct.201802836>.
- [24] N. Zhang, D. Chen, F. Niu, S. Wang, L. Qin, Y. Huang, Enhanced visible light photocatalytic activity of Gd-doped BiFeO₃ nanoparticles and mechanism insight, *Sci. Rep.* 6 (2016) 1–11, <https://doi.org/10.1038/srep26467>.
- [25] Q. Xiang, J. Yu, P.K. Wong, Quantitative characterization of hydroxyl radicals produced by various photocatalysts, *J. Colloid Interface Sci.* 357 (2011) 163–167, <https://doi.org/10.1016/j.jcis.2011.01.093>.
- [26] W. Yu, J. Chen, T. Shang, L. Chen, L. Gu, T. Peng, Direct Z-scheme g-C₃N₄/WO₃ photocatalyst with atomically defined junction for H₂ production, *Appl. Catal. B Environ.* 219 (2017) 693–704, <https://doi.org/10.1016/j.apcatb.2017.08.018>.
- [27] T.C. Sabari Girisun, M. Saravanan, V.R. Soma, Wavelength-dependent nonlinear optical absorption and broadband optical limiting in Au-Fe₂O₃-rGO nanocomposites, *ACS Appl. Nano Mater.* 1 (2018) 6337–6348, <https://doi.org/10.1021/acsnano.8b01544>.
- [28] P.S. Veluri, A. Shaligram, S. Mitra, Porous α -Fe₂O₃ nanostructures and their lithium storage properties as full cell configuration against LiFePO₄, *J. Power Sources* 293 (2015) 213–220, <https://doi.org/10.1016/j.jpowsour.2015.05.071>.
- [29] S. Shahajan, P. Arumugam, R. Rajendran, A. PonnuSamy Munusamy, Optimization and detailed stability study on Pb doped ceria nanocubes for enhanced photodegradation of several anionic and cationic organic pollutants, *Arab. J. Chem.* (2017), <https://doi.org/10.1016/j.arabjc.2017.11.001>.
- [30] H. Zhang, X. Sun, X. Huang, L. Zhou, Encapsulation of α -Fe₂O₃ nanoparticles in graphitic carbon microspheres as high-performance anode materials for lithium-ion batteries, *Nanoscale.* 7 (2015) 3270–3275, <https://doi.org/10.1039/c4nr06771a>.
- [31] J. Xu, Z. Wang, Y. Zhu, Enhanced visible-light-driven photocatalytic disinfection performance and organic pollutant degradation activity of porous g-C₃N₄ nanosheets, *ACS Appl. Mater. Interfaces* 9 (2017) 27727–27735, <https://doi.org/10.1021/acsami.7b07657>.
- [32] X. Sun, D. Jiang, L. Zhang, W. Wang, Alkaline modified g-C₃N₄ photocatalyst for high selective oxide coupling of benzyl alcohol to benzoquinone, *Appl. Catal. B Environ.* 220 (2018) 553–560, <https://doi.org/10.1016/j.apcatb.2017.08.057>.
- [33] J. Wang, L. Tang, G. Zeng, Y. Deng, Y. Liu, L. Wang, Y. Zhou, Z. Guo, J. Wang,

- C. Zhang, Atomic scale g-C₃N₄/Bi₂WO₆ 2D/2D heterojunction with enhanced photocatalytic degradation of ibuprofen under visible light irradiation, *Appl. Catal. B Environ.* 209 (2017) 285–294, <https://doi.org/10.1016/j.apcatb.2017.03.019>.
- [34] Y. Yao, C. Xu, S. Yu, D. Zhang, S. Wang, Facile synthesis of Mn₃O₄-reduced graphene oxide hybrids for catalytic decomposition of aqueous organics, *Ind. Eng. Chem. Res.* 52 (2013) 130226103026006, , <https://doi.org/10.1021/ie303220x>.
- [35] Y. Xu, S. Huang, M. Xie, Y. Li, L. Jing, H. Xu, Q. Zhang, H. Li, Core-shell magnetic Ag/AgCl@Fe₂O₃ photocatalysts with enhanced photoactivity for eliminating bisphenol A and microbial contamination, *New J. Chem.* 40 (2016) 3413–3422, <https://doi.org/10.1039/C5NJ02898A>.
- [36] D. Channei, B. Inceesungvorn, N. Wetchakun, S. Ukritnukun, A. Nattestad, J. Chen, S. Phanichphant, Photocatalytic degradation of methyl orange by CeO₂ and Fe-doped CeO₂ films under visible light irradiation, *Sci. Rep.* 4 (2014), <https://doi.org/10.1038/srep05757>.
- [37] J. You, Y. Xiang, Y. Ge, Y. He, Synthesis of Ternary rGO-ZnO-Fe₃O₄ Nanocomposites and Their Application for Visible Light Photocatalytic Degradation of Dyes, (2017), pp. 2161–2169, <https://doi.org/10.1007/s10098-017-1385-2>.
- [38] S. Gupta, V. Subramanian, Encapsulating Bi₂Ti₂O₇(BTO) with reduced graphene oxide (RGO): An effective strategy to enhance photocatalytic and photoelectrocatalytic activity of BTO, *ACS Appl. Mater. Interfaces* 6 (2014) 18597–18608, <https://doi.org/10.1021/am503396r>.
- [39] C. Xue, H. An, X. Yan, J. Li, B. Yang, J. Wei, G. Yang, Spatial charge separation and transfer in ultrathin CdIn₂S₄/rGO nanosheet arrays decorated by ZnS quantum dots for efficient visible-light-driven hydrogen evolution, *Nano Energy* 39 (2017) 513–523, <https://doi.org/10.1016/j.nanoen.2017.07.030>.
- [40] J. Hou, S. Jiao, H. Zhu, R.V. Kumar, Carbon-modified bismuth titanate nanorods with enhanced visible-light-driven photocatalytic property, *CrystEngComm.* 13 (2011) 4735, <https://doi.org/10.1039/c1ce05409k>.
- [41] L. Bo, J. Li, B. Xu, X. Yan, B. Yang, J. Wei, G. Yang, Spatial positioning effect of dual cocatalysts accelerating charge transfer in three dimensionally ordered macro-porous g-C₃N₄ for photocatalytic hydrogen evolution, *Appl. Catal. B* 243 (2019) 94–105, <https://doi.org/10.1016/j.apcatb.2018.10.029>.
- [42] Z. Ji, X. Shen, J. Yang, G. Zhu, K. Chen, A novel reduced graphene oxide/Ag/CeO₂ ternary nanocomposite: green synthesis and catalytic properties, *Appl. Catal. B Environ.* 144 (2014) 454–461, <https://doi.org/10.1016/j.apcatb.2013.07.052>.
- [43] S. Dutta, R. Sahoo, C. Ray, S. Sarkar, J. Jana, Y. Negishi, T. Pal, Biomolecule-mediated CdS-TiO₂ -reduced graphene oxide ternary nanocomposites for efficient visible light-driven photocatalysis, *Dalton Trans.* 44 (2015) 193–201, <https://doi.org/10.1039/C4DT02749C>.
- [44] A.A. Al-Kahtani, Photocatalytic degradation of rhodamine B dye in wastewater using gelatin/CuS/PVA nanocomposites under solar light irradiation, *J. Biomater. Nanobiotechnol.* 08 (2017) 66–82, <https://doi.org/10.4236/jbnb.2017.81005>.
- [45] X.L. Luo, M.J. Wang, D.S. Yang, J. Yang, Y.S. Chen, Hydrothermal synthesis of morphology controllable Cu₂O and their catalysis in thermal decomposition of ammonium perchlorate, *J. Ind. Eng. Chem.* 32 (2015) 313–318, <https://doi.org/10.1016/j.jiec.2015.09.015>.
- [46] T.S. Natarajan, M. Thomas, K. Natarajan, H.C. Bajaj, R.J. Tayade, Study on UV-LED/TiO₂ process for degradation of Rhodamine B dye, *Chem. Eng. J.* 169 (2011) 126–134, <https://doi.org/10.1016/j.cej.2011.02.066>.
- [47] J. Madhavan, F. Grieser, M. Ashokkumar, Combined advanced oxidation processes for the synergistic degradation of ibuprofen in aqueous environments, *J. Hazard. Mater.* 178 (2010) 202–208, <https://doi.org/10.1016/j.jhazmat.2010.01.064>.
- [48] X. Zhou, Z. Liu, Y. Wang, Y. Ding, Facet effect of Co₃O₄ nanocrystals on visible-light driven water oxidation, *Appl. Catal. B Environ.* 237 (2018) 74–84, <https://doi.org/10.1016/j.apcatb.2018.05.067>.
- [49] Y. Zhao, H. Fan, K. Fu, L. Ma, M. Li, J. Fang, Intrinsic electric field assisted polymeric graphitic carbon nitride coupled with Bi₄Ti₃O₁₂/Bi₂Ti₂O₇ heterostructure nanofibers toward enhanced photocatalytic hydrogen evolution, *Int. J. Hydrogen Energy* 41 (2016) 16913–16926, <https://doi.org/10.1016/j.ijhydene.2016.07.162>.
- [50] L. Jinhai, M. Han, Y. Guo, F. Wang, L. Meng, D. Mao, S. Ding, C. Sun, Hydrothermal synthesis of novel flower-like BiVO₄/Bi₂Ti₂O₇ with superior photocatalytic activity toward tetracycline removal, *Appl. Catal. A Gen.* 524 (2016) 105–114, <https://doi.org/10.1016/j.apcata.2016.06.025>.
- [51] T. Chen, Q. Hao, W. Yang, C. Xie, D. Chen, C. Ma, W. Yao, Y. Zhu, A honeycomb multilevel structure Bi₂O₃ with highly efficient catalytic activity driven by bias voltage and oxygen defect, *Appl. Catal. B Environ.* 237 (2018) 442–448, <https://doi.org/10.1016/j.apcatb.2018.05.044>.
- [52] A.D. Liyanage, S.D. Perera, K. Tan, Y. Chabal, K.J. Balkus, Synthesis, Characterization, and Photocatalytic Activity of Y-Doped CeO₂ Nanorods, *ACS Catal.* 4 (2014) 577–584, <https://doi.org/10.1021/cs400889y>.
- [53] M. Joy, A.P. Mohamed, K.G.K. Warrier, U.S. Hareesh, Visible-light-driven photocatalytic properties of binary MoS₂ /ZnS heterostructured junctions synthesized via one-step hydrothermal route, *New J. Chem.* 41 (2017) 3432–3442, <https://doi.org/10.1039/C6NJ03727E>.
- [54] P. Wang, Y. Sheng, F. Wang, H. Yu, Synergistic effect of electron-transfer mediator and interfacial catalytic active-site for the enhanced H₂-evolution performance: a case study of CdS-Au photocatalyst, *Elsevier B.V.* (2018), <https://doi.org/10.1016/j.apcatb.2017.08.080>.
- [55] N. Lu, P. Wang, Y. Su, H. Yu, N. Liu, X. Quan, Construction of Z-Scheme g-C₃N₄/RGO/WO₃ With in Situ Photoreduced Graphene Oxide As Electron Mediator for Efficient Photocatalytic Degradation of Ciprofloxacin, (2019), <https://doi.org/10.1016/j.chemosphere.2018.10.065>.
- [56] C. Lai, M. Zhang, B. Li, D. Huang, G. Zeng, L. Qin, X. Liu, H. Yi, M. Cheng, L. Li, Z. Chen, L. Chen, Fabrication of CuS/BiVO₄ (0 4 0) binary heterojunction photocatalysts with enhanced photocatalytic activity for Ciprofloxacin degradation and mechanism insight, *Chem. Eng. J.* 358 (2019) 891–902, <https://doi.org/10.1016/j.cej.2018.10.072>.